remote sensing

MDPI

Article

Spectral Variability and Prediction of Nitrogen, Phosphorus, and Potassium in Fresh Sugarcane (*Saccharum officinarum*) Leaves by VIS–NIR–SWIR Spectroscopy

Marta Laura de Souza Alexandre, Izabelle de Lima e Lima, Carlos Augusto Alves Cardoso Silva, Mateus Lima Silva *, Rodnei Rizzo and Peterson Ricardo Fiorio

Department of Biosystems Engineering, "Luiz de Queiroz" College of Agriculture, University of São Paulo, Piracicaba 13418900, SP, Brazil; martalaura@usp.br (M.L.d.S.A.); eng.izabellelima@usp.br (I.d.L.e.L.); carlosesalq@usp.br (C.A.A.C.S.); rodnei.rizzo@usp.br (R.R.); fiorio@usp.br (P.R.F.)
* Correspondence: mateuslima.silva@usp.br

Highlights

What are the main findings?

- VIS–NIR–SWIR leaf spectroscopy proved effective for predicting nitrogen (R^2 = 0.83) and phosphorus (R^2 = 0.80) under the seasonal conditions observed in 2024/2025 but showed limited performance for potassium (R^2 = 0.25) due to the absence of specific absorption features.
- The spectral variability of sugarcane was predominantly modulated by seasonal factors, particularly rainfall regime, and phenological factors, whereas the genetic effect among varieties was considered secondary.

What are the implications of the main findings?

- To ensure the stability and spatiotemporal generalization of spectral models across growing seasons, future studies should incorporate continuous auxiliary variables related to crop phenology and, when possible, direct measurements of foliar water status.
- The spectral variability of sugarcane was predominantly modulated by seasonal factors (water regime) and phenological factors, whereas the genetic effect among varieties was considered secondary.

Abstract

This study evaluated the potential of VIS–NIR–SWIR leaf spectroscopy to predict N, P, and K contents in sugarcane, considering spectral variability across two growing seasons (2023/2024 and 2024/2025), phenological stages, and five varieties. Spectral signatures (350–2500 nm) were acquired using a FieldSpec 3 spectroradiometer and processed with MSC, smoothing, and the first Savitzky–Golay derivative. Diagnostic bands were identified by Spearman correlation, and prediction was performed using partial least squares regression (PLSR). PCA showed that spectral variability was driven mainly by seasonal and phenological factors, whereas varietal effects were secondary. In 2023/2024, greater spectral homogeneity was associated with lower predictive performance. In 2024/2025, greater spectral heterogeneity was associated with improved prediction for N (R^2 = 0.83; RMSE = 0.78 g kg^{-1}) and P (R^2 = 0.80; RMSE = 0.10 g kg^{-1}). Potassium remained the most challenging nutrient to predict (maximum R^2 = 0.25), mainly due to its ionic nature and the resulting lack of significant correlation with specific VIS, NIR, and SWIR spectral features. These results indicate strong potential for predicting N and P in fresh sugarcane leaves, although model robustness depends on the extent of spectral variability in the dataset.

Check for updates

Academic Editors: Xiaoyang Zhang, Hans-Peter Kaul and Abid Ali

Received: 23 March 2026
Revised: 18 April 2026
Accepted: 28 April 2026
Published: 7 July 2026

Copyright: © 2026 by the authors. Licensee MDPI, Basel, Switzerland. This article is an open access article distributed under the terms and conditions of the Creative Commons Attribution (CC BY) license.

Keywords: nutrients; machine learning; PLSR; spectral signatures

1. Introduction

Due to its efficient photosynthetic metabolism (C4 pathway) and long developmental cycle, sugarcane requires large amounts of soil nutrients, as well as ample water availability and solar radiation, to express its maximum productive potential [1,2]. Therefore, sugarcane nutritional management requires rapid, reproducible, and scalable diagnostic approaches.

Remote sensing based on reflectance spectroscopy has emerged as a promising tool for monitoring crop nutritional status [3]. From a physical-optical perspective, the leaf spectral response across the 300–2500 nm range can be understood in three functional regions: VIS, predominantly associated with pigments; NIR, mainly related to cellular structure; and SWIR, characterized by water absorption in leaf tissue, but also containing features linked to proteins, nitrogenous compounds, and structural carbon-based constituents such as cellulose, lignin, sugars, and starch [4,5]. This foundation supports the integrated use of VIS–NIR–SWIR signatures for investigating foliar macronutrients.

The spectral response of fresh leaves in the VIS–NIR–SWIR range has potential for estimating plant nutritional status because it reflects biochemical and structural variations in leaf tissue across different spectral regions [6,7]. However, the performance of spectral models depends on both intrinsic leaf attributes, such as water content, pigments, and leaf structure, and on methodological factors, such as sample collection, storage, and preprocessing, all of which directly influence this spectral response [8,9]. This aspect becomes particularly relevant in foliar nutrient prediction, since the signals associated with N, P, and K are not expressed with the same intensity and specificity across the spectrum.

Nitrogen accounts for approximately 1% of sugarcane phytomass, and its deficiency impairs chlorophyll and amino acid synthesis, reduces photosynthetic rate, and negatively affects growth and yield [10]. Proper nitrogen (N) management is associated with gains in sugarcane productivity [11,12], although responses depend on dose, variety, and edaphoclimatic conditions. From a spectral standpoint, these effects tend to be manifested in the VIS and red-edge regions, which explains the strong performance of green, red-edge, and NIR indices for estimating chlorophyll and N [13].

In contrast, the spectral detection of phosphorus (P) and potassium (K) in fresh leaves is more complex, since these nutrients are not as directly associated with optically active compounds as N. In the case of P, its roles in ATP synthesis, sugar metabolism, cell division, and sucrose accumulation influence plant development and function [14], but its spectral effects tend to occur indirectly through physiological and structural changes in the tissue. Its deficiency results in reduced growth, lower tillering, narrow leaves, and restricted root system development [15], characteristics that may alter spectral response in a subtler and less specific manner.

Similarly, K plays an essential role in osmotic regulation, plant metabolism, and the efficiency of N and water use [16]. Although sugarcane exports greater amounts of K than N, the management of this nutrient remains frequently neglected [17]. In optical terms, the effects of P and K tend to be less direct and more diffuse, as they arise from physiological and structural changes in fresh leaf tissue rather than being associated with strongly diagnostic spectral features, and may be subtly expressed in different spectral regions, including 350–730 nm and 1420–1800 nm [18]. In fresh leaves, this interpretation becomes even more challenging due to the influence of water on the spectral signature, which may partially mask the effects of these nutrients and reduce the specificity of the signals associated with them [19].

From an applied perspective, this greater complexity does not reduce the relevance of analysis in fresh tissue. In sugarcane, N prediction in fresh leaves using VIS–NIR–SWIR achieved an R^2 of 0.72 [6], whereas in fresh citrus leaves, P and K reached R^2 values of 0.60 and 0.63, respectively [20], demonstrating predictive feasibility, although with more moderate performance. This behavior contrasts with studies using dried and ground leaves, in which water removal and greater material homogenization tend to increase model accuracy, with R^2 values ranging from 0.76 to 0.98 for macronutrients in cotton, in addition to better performance of ground material compared with intact dried leaves in maize and sorghum [21,22]. Even so, analysis in fresh leaves preserves the physiological condition of the plant at the time of sampling and requires less sample preparation, favoring faster and more operational field applications [20]. Although the literature remains largely concentrated on N [6,7,23–25], the spectral relationships associated with P and K in fresh sugarcane leaves still require greater consistency and validation. In this sense, this gap highlights the relevance of exploring the foliar spectral behavior of P and K in sugarcane, contributing to the consolidation of more robust diagnostic foundations and to the advancement of spectral applications in crop nutritional monitoring.

Accordingly, the objective of this study was to evaluate the potential of VIS–NIR–SWIR leaf spectroscopy for predicting nitrogen, phosphorus, and potassium contents in fresh sugarcane leaves, by analyzing the spectral variability associated with harvest seasons, developmental stages, and varieties, as well as its implications for spectral modeling. Thus, this study sought to determine whether reflectance spectroscopy is effective for estimating P and K through indirect associations, and to identify which spectral ranges retain relevant information for detecting diagnostic spectral regions correlated with these macronutrients.

2. Materials and Methods

In this study, the methodology was structured to predict nitrogen (N), phosphorus (P), and potassium (K) contents in fresh sugarcane leaves. The main approach consisted of spectral acquisition and analysis of the samples, with emphasis on identifying the spectral regions most influential for estimating these nutrients. The methodology adopted in this study comprised six main stages: (i) definition of the study area; (ii) acquisition of leaf material; (iii) laboratory analysis to determine N, P, and K contents; (iv) acquisition of hyperspectral data; (v) data processing; and (vi) prediction of NPK contents (Figure 1).

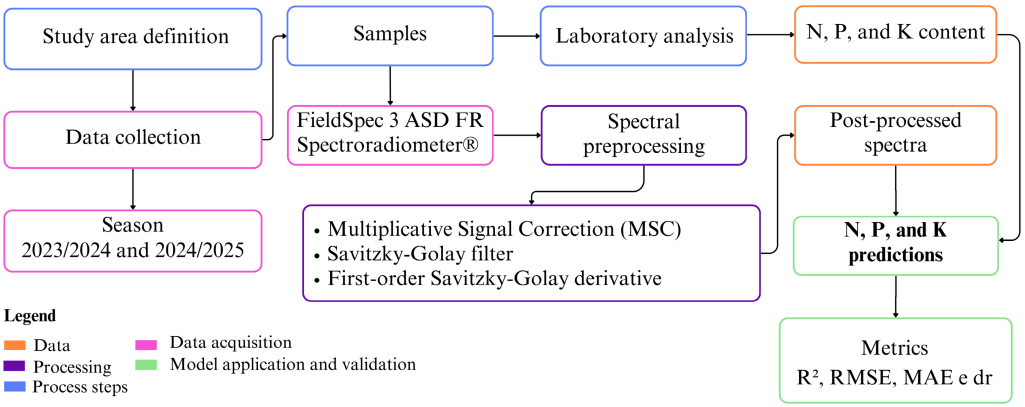

Figure 1. Methodological flowchart of the study.

2.1. Study Area

The experiment was conducted in the municipality of Piracicaba, São Paulo, Brazil, located at 22°42′15″ south latitude and 47°33′34″ west longitude, at the facilities of the Sugarcane Technology Center (CTC) (Figure 2). The soil in the experimental area is classified

as a very clayey Red-Yellow Ultisol. The region has a humid subtropical climate (CWa), with mean annual precipitation below 1400 mm, characterized by rainy summers and dry winters [26].

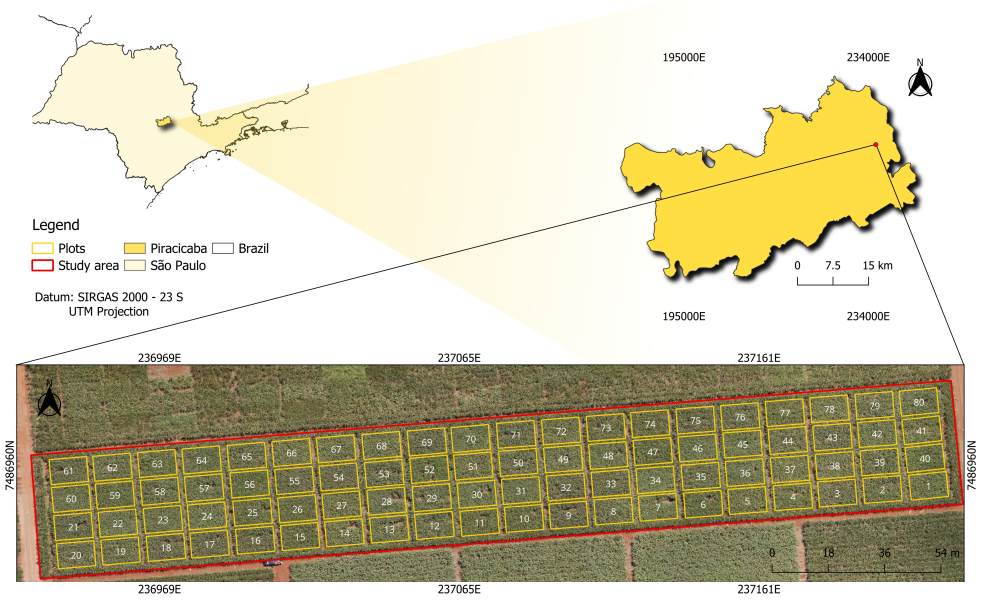

Figure 2. Location map of the study area.

2.2. Experimental Description

The experimental design used was a randomized complete block design (RCBD) in a factorial arrangement, with four experimental blocks. The interaction between five sugarcane varieties and four fertilization regimes was analyzed, totaling 80 experimental plots. The plots, consisting of 6 rows that were 12 m long and 6 m wide, were subjected to different fertilization treatments, with NPK sources applied under the following regimes: (i) control (without fertilizer application), (ii) conventional fertilization, (iii) optimized fertilization 1, and (iv) optimized fertilization 2 (Table 1).

Table 1. Alternating fertilizer rates for the 2022/2023 planting, 2023/2024 ridge-breaking stage, and ratoon crops (2024/2025).

Treatments	Planting			Ridge Breaking		Ratoon		
	N	P_2O_5	K_2O	N	K_2O	N	P_2O_5	K_2O
	kg ha^{-1}					kg t^{-1}		
T1—Control	-	-	-	-	-	-	-	-
T2—Conventional	40	120	120	-	-	1.0	0.2	1.0
T3—Optimized 1	40	180	80	30	80	1.2	0.4	1.2
T4—Optimized 2	40	200	80	50	140	1.2	0.6	1.6

Fertilizer doses were applied manually at the three main cultivation stages: planting, ridge breaking (planting furrow leveling), and ratoon crops (adjusted according to the average yield per plot). NPK management was maintained over three consecutive production cycles (2023/2024, 2024/2025, and 2025/2026), with specific adjustments for each sugarcane variety.

2.3. Leaf Sampling

Leaf sampling was performed by collecting six +1 leaves (the first fully expanded leaf from the top downward with a visible auricle) per plot. Sampling was carried out during the morning period (08:00–10:00) in order to minimize environmental variation.

For modeling purposes, the spectral signatures of these six leaves were consolidated into a single representative signature per plot using the median value. Consequently, the final dataset used for modeling consisted of 240 samples for the 2023/2024 season and 240 samples for the 2024/2025 season, totaling 480 samples used in the study.

After collection, the leaves were placed in plastic bags, stored in insulated boxes with ice, and then transported to the laboratory, where spectral readings were performed [8,27]. Sampling was conducted over two growing seasons, 2023/2024 and 2024/2025, following crop development from the vegetative growth stage, expressed as days after cutting (DAC) (Table 2).

Table 2. Growing seasons, crop stages, and leaf sampling times expressed as days after cutting (DAC).

Growing Season	Stage	Sampling Times (DAC)
2023/2024	First ratoon cane	1st (180), 2nd (220), 3rd (320)
2024/2025	Second ratoon cane	4th (220), 5th (290), 6th (350)

2.4. Spectral Data Acquisition

In the laboratory, spectral readings of the leaves were performed on the middle third of the leaf blade, on the adaxial surface, while avoiding the central vein. Spectral signatures of fresh leaves were obtained using a FieldSpec 3 ASD FR Spectroradiometer® (ASD Inc., Boulder, CO, USA) [28], which operates within the spectral range of 350 to 2500 nm, with a resolution of 1.4 nm from 350 to 1050 nm and 2 nm from 1050 to 2500 nm. For the measurements, the sensor was coupled to a Leaf Clip® probe (ASD Inc., Boulder, CO, USA) [28], ensuring constant light incidence and intensity in all readings and thus providing fully controlled conditions.

The spectrometer remained powered on for 30 min prior to measurements to warm up and stabilize the instrument's halogen lamp. Calibration with a Lambertian panel was repeated every 20 readings and whenever instrumental drift was detected (Figure 3). After spectral readings of the fresh leaves, the samples were dried in a forced-air oven at 65 °C until constant weight was reached, then ground and sent for chemical analysis.



Figure 3. Step-by-step methodological procedures for leaf acquisition and subsequent spectral readings prior to chemical analysis.

2.5. Spectral Preprocessing

The data obtained from leaf spectral readings were subjected to preprocessing to correct inconsistencies in the measurements caused by external factors, such as environmental variation and light scattering [29].

Preprocessing was divided into three parts: (i) removal of wavelengths from 350 to 404 nm due to the high concentration of noise observed; (ii) application of the Multiplicative Scatter Correction (MSC) function; and (iii) application of the Savitzky–Golay (SG) smoothing filter [30], used exclusively as a smoothing technique to reduce high-frequency noise while preserving the original spectral shape. These preprocessing steps were performed in ParLeS software version 3.1. The formulas used to correct the spectra using the MSC method are presented below.

$$\text{Spectra}_{\text{avg}} = \frac{\sum_1^n \text{Spectra}_i}{n} \quad (1)$$

$$\text{Spectra}_i = K_i \times \text{Spectra}_{\text{avg}} + b_i \quad (2)$$

$$\text{Spectra}_{\text{MSC},i} = \frac{\text{Spectra}_i - b_i}{k_i} \quad (3)$$

where $\text{Spectra}_{\text{avg}}$ represents the average of all leaf spectra, n is the total number of spectral data points, and Spectra_i corresponds to each individual leaf spectrum. The coefficients k_i and b_i are correction parameters obtained by linear regression based on $\text{Spectra}_{\text{avg}}$, and $\text{Spectra}_{\text{MSC},i}$ is the resulting spectrum after MSC.

2.6. First-Order Savitzky–Golay Derivative

To eliminate baseline variations resulting from additive light-scattering effects and to enhance overlapping absorption features, the first derivative was applied to the reflectance spectra. Processing was performed using the Savitzky–Golay [30] algorithm, implemented through the prospectr package in the R computing environment [31]. At this stage, a second-order polynomial was applied over a moving window of 35 points (w = 35).

Because derivative transformations are sensitive to high-frequency noise, the moving window size must be defined as a trade-off between noise attenuation and the preservation of meaningful spectral features. In this study, the configuration of w = 35 was adopted because it provided stable derivative spectra for subsequent PLSR modeling, preserving the slope of broad biochemical absorption bands while reducing local spectral noise. The literature emphasizes that derivative preprocessing should be accompanied by appropriate smoothing, and that Savitzky–Golay parameters are typically defined empirically, varying according to spectral resolution, sample characteristics, and the noise structure of the dataset [32,33].

Derivatives represent the variation in reflectance as a function of wavelength and help reduce noise caused by sample geometry and roughness [34]. By minimizing these scattering effects, the technique promotes the robustness required for reliable estimation of agronomic parameters [35].

2.7. Spearman Correlation

Spearman correlation was used to identify the spectral ranges most sensitive to variations in leaf nitrogen, phosphorus, and potassium contents. This technique evaluates monotonic relationships and performs well when applied to nonlinear data [36]. The results made it possible to map the regions of the electromagnetic spectrum (VIS, NIR, and SWIR) associated with the crop's nutritional status, serving as a basis for interpreting the predictive models [22]. For analytical purposes, strong correlations were those with absolute coefficients equal to or greater than ($|r| \geq 0.7$), indicating a consistent association between the optical response and the agronomic variable. Correlation coefficient values range from −1 to +1, indicating negative and positive correlation, respectively.

2.8. Reference Chemical Analyses

After spectral readings of the fresh leaves were completed, the samples were separated by plot and subsequently sent for chemical analysis of N, P, and K. After drying, grinding, and digestion of the plant samples, nutrient contents were determined using the following methods: Semi-Micro-Kjeldahl for N, metavanadate colorimetry for P, and flame emission photometry for K [37].

2.9. Predictive Modeling with PLSR

Partial Least Squares Regression (PLSR) was used to build predictive models for leaf N, P, and K contents. This algorithm is widely used in chemometrics and hyperspectral remote sensing due to its ability to efficiently handle multicollinearity, an intrinsic phenomenon in spectral data in which adjacent bands are highly correlated with one another [38].

Modeling was performed in the R statistical environment [31] using the pls package. To assess model robustness and prevent overfitting, 10-fold cross-validation (k = 10) was employed. The optimal number of latent variables (LVs) for each model was automatically determined based on the cross-validation results. This procedure was specifically used to identify the number of factors that minimized the Root Mean PRESS statistic, thereby optimizing predictive performance and model generalizability.

2.10. Model Validation

Model performance was evaluated using performance metrics such as the coefficient of determination (R^2), root mean square error (RMSE), and mean absolute error (MAE), described in Equations (4)–(6). To test agreement, the Willmott index (d) was also used, which reflects the degree to which measured data are accurately estimated by predicted data, as presented in Equation (7).

$$R^2 = \sum_{i=1}^{n}(\hat{y}_i - \overline{y}\,)^2 / \sum_{i=1}^{n}(\hat{y}_i - \overline{y}\,)^2 \quad (4)$$

$$RMSE = \sqrt{\frac{\sum_{i=1}^{n}(\hat{y}_i - y_i\,)^2}{n}} \quad (5)$$

$$\mathrm{MAE} = \frac{1}{\mathrm{n}}\sum_{\mathrm{i}=1}^{\mathrm{n}}|\hat{y}_i - \overline{y}| \quad (6)$$

$$\mathrm{d} = 1 - \frac{\sum_{\mathrm{i}=1}^{\mathrm{n}}(\hat{y}_i - \mathrm{y_i})^2}{\sum_{\mathrm{i}=1}^{\mathrm{n}}(|\hat{y}_i - \overline{y}\,| + |\,\hat{y}_i - \overline{y}\,|)^2} \quad (7)$$

where $\hat{\mathrm{y}}_\mathrm{i}$ and y_i represent the predicted and observed nutrient concentrations of the *i*-th sample, respectively; $\overline{y}$ represents the arithmetic mean of the observed values; and n is the total number of samples.

3. Results

3.1. Rainfall Conditions Throughout Crop Development and Changes in Foliar N, P, and K Concentrations

The rainfall conditions observed over the two growing seasons showed distinct patterns. This contrast was directly reflected in crop phenology, especially in the timing of entry into the stage of maximum vegetative growth. While in the 2023/2024 growing season the first sampling was performed 180 days after cutting (DAC), in the 2024/2025 growing season this same phenological stage was only reached at 220 DAC, indicating a delay in crop development imposed by the environmental constraints of the second cycle.

The 2023/2024 growing season was characterized by lower-than-expected rainfall, although it was well distributed during the initial periods of vegetative crop development. In some months, such as October 2023 and March 2024, precipitation above the historical average was recorded (Figure 4), corresponding to the periods when the first and third samplings were carried out. The second sampling showed lower-than-expected rainfall volumes, indicating a water deficit. In the 2024/2025 growing season, a water deficit was observed virtually from June to October, which was reflected in delayed vegetative development and, consequently, in the phenological stages and the temporal schedule of data collection (Figure 4).

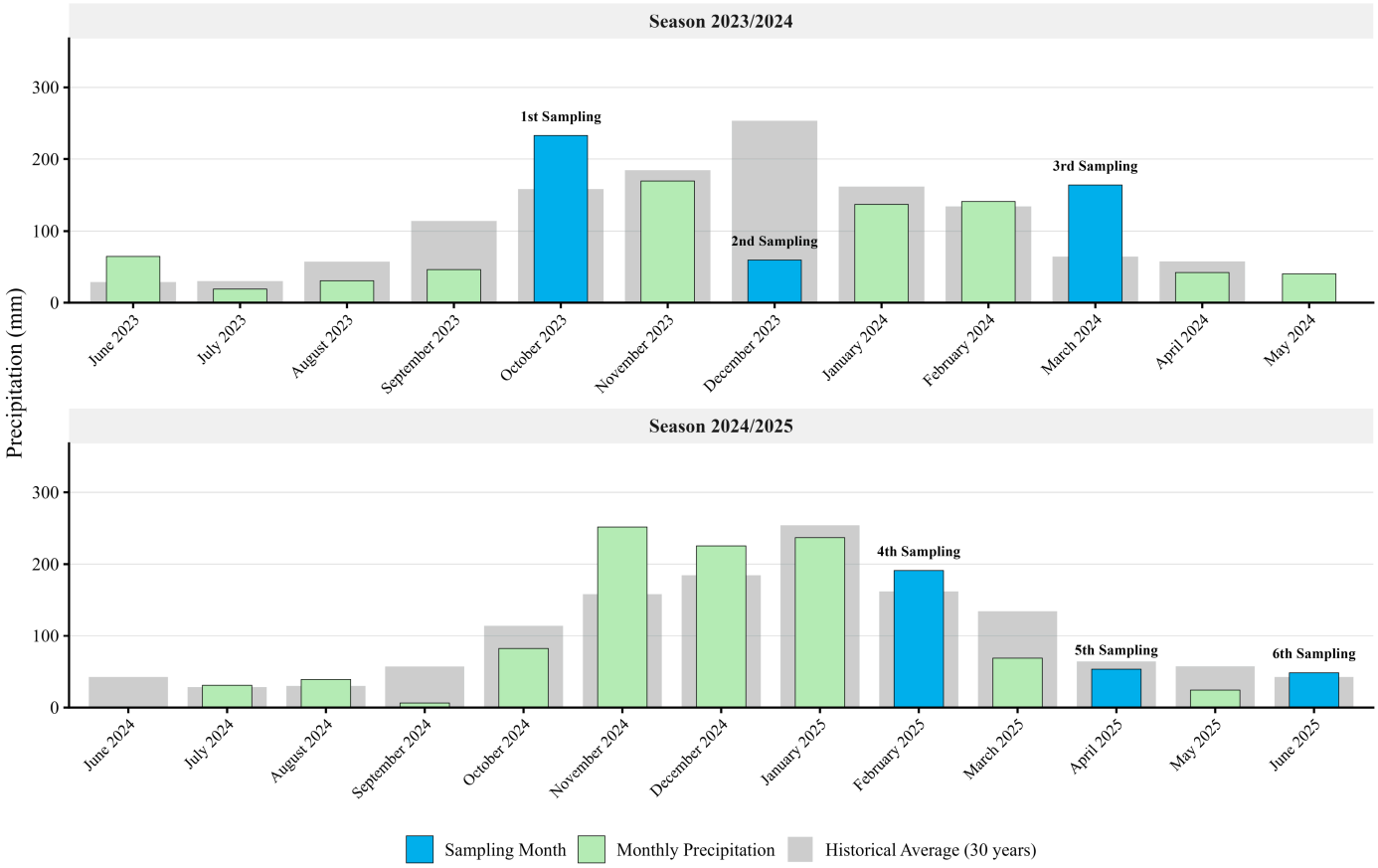

Figure 4. Monthly rainfall observed during the 2023/2024 and 2024/2025 growing seasons compared with the historical average (30 years) for the municipality of Piracicaba, SP. The green bars represent the monthly rainfall observed in each growing season, whereas the gray bars indicate the historical average. The sampling months are highlighted in blue tones and identified as the 1st to the 6th sampling. Harvests were carried out on 26 June 2024, and 20 June 2025.

These differences indicate that the leaf samples were collected under contrasting seasonal rainfall conditions, which may have influenced the spectral signature of the leaves. During rainier periods, the spectral response may be more strongly influenced by water-related absorption features, especially in the SWIR region, and this context is consistent with changes in spectral response, especially in the SWIR region, where water exhibits marked absorption features. In contrast, samplings performed under reduced rainfall conditions may promote increased reflectance in these regions (NIR and SWIR) which may be associated with reduced water-related spectral influence and changes in leaf optical behavior, as a result of the interaction of electromagnetic energy with the spongy mesophyll, which is responsible for radiation scattering [39]. In this tissue, multiple reflections and

refractions of electromagnetic radiation occur, associated with differences between the refractive indices of air (1.0) and water (1.4) [40].

This rainfall distinction suggests that seasonal environmental conditions were among the main factors associated with the quality and variability of the spectral data. Under these conditions, delayed vegetative development may also have contributed to the observed variability, directly affecting nutrient uptake and the variability of the observed data. For a coherent analysis, leaf samplings should be interpreted from the perspective of the crop phenological stages: the first sampling of each growing season represents the peak of vegetative growth (1st and 4th samplings); the second sampling indicates the onset of ripening development (2nd and 5th samplings); and the third reflects the period close to the end of ripening and harvest (3rd and 6th samplings).

Accordingly, the first and fourth samplings carried out in this study occurred at the stage of maximum vegetative growth, the period during which the highest nutrient concentrations in the plant are expected [41]. Figure 5 illustrates the evolution of foliar macronutrient concentrations throughout these phases. In the 2023/2024 growing season, nitrogen showed the highest foliar concentrations in the initial samplings, followed by a progressive reduction in the 3rd sampling.

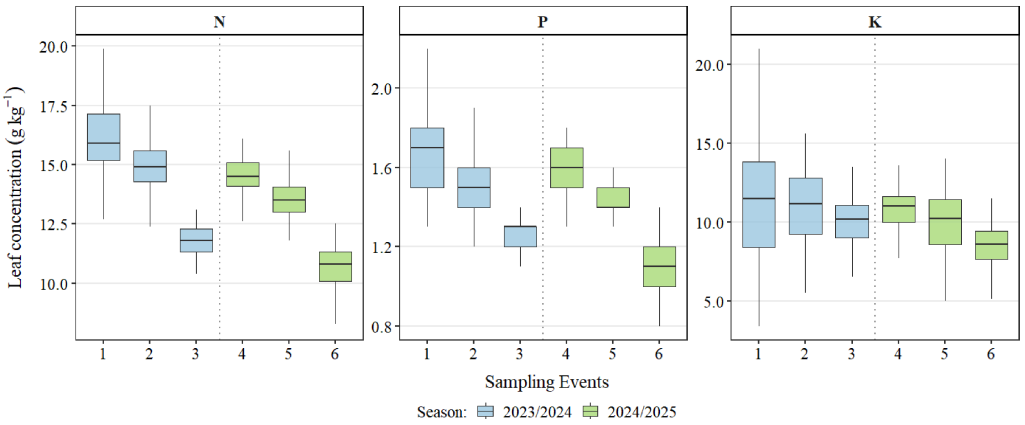

Figure 5. Boxplot analysis of the foliar concentrations of the macronutrients nitrogen, phosphorus, and potassium. Events 1, 2, and 3 correspond to the three independent data collection campaigns conducted during the 2023/2024 growing season (blue). Similarly, events 4, 5, and 6 correspond to the three campaigns carried out during the 2024/2025 growing season (green). The vertical dashed line explicitly separates the two growing seasons.

The 2024/2025 growing season showed median values lower than those of the previous growing season. In addition, the lower rainfall observed in the initial period may have contributed to delayed vegetative development. Consequently, the first leaf sampling of this cycle (corresponding to the 4th overall sampling) occurred only 7 months after cutting (July–January). The boxplots show median N contents lower than those of the first sampling of the 2023/2024 growing season, suggesting delayed crop development in this cycle. This factor explains the distinct dynamics of N uptake in the two growing seasons.

This pattern of greater initial variation followed by subsequent stabilization also extends to phosphorus (P) and potassium (K) contents. In general, a greater amplitude of values was observed in the 2023/2024 growing season, whereas narrower ranges were found in the 2024/2025 growing season. For phosphorus, the range of variation was smaller than that of nitrogen, indicating greater foliar stability throughout the cycle, with gradual median reductions until the sixth sampling. Potassium, in turn, exhibited the greatest relative variability, especially in the initial samplings of the 2023/2024 growing season, as evidenced by the high dispersion of the data and the presence of maximum values. In the

2024/2025 growing season, the reduced dispersion and lower median K values corroborate the restrictive impact of the initial delay in vegetative development. A structured and continuous decline in potassium medians can be observed from the first sampling of this cycle (4th sampling) through the progression of ripening (6th sampling).

3.2. Spectral Variation Throughout Crop Development

The global principal component analysis (PCA) (Figure 6) revealed distinct patterns of spectral variation as a function of growing season, evaluated varieties, and developmental stages (DAC). In the plot referring to growing seasons (Figure 6A), partial overlap between groups was observed along the first principal component (PC1), whereas the distinction between growing seasons became more evident in the second principal component (PC2), in addition to differences in data dispersion. The 2023/2024 growing season, characterized by seasonal conditions more favorable to crop development, exhibited a smaller amplitude of spectral variation, with points more concentrated along the PC2 axis. In contrast, the 2024/2025 growing season showed significantly greater data dispersion along the PC2 axis. This behavior is consistent with the impact of water deficit during the first months of development, which may have contributed to delayed vegetative growth and greater spectral heterogeneity throughout the cycle.

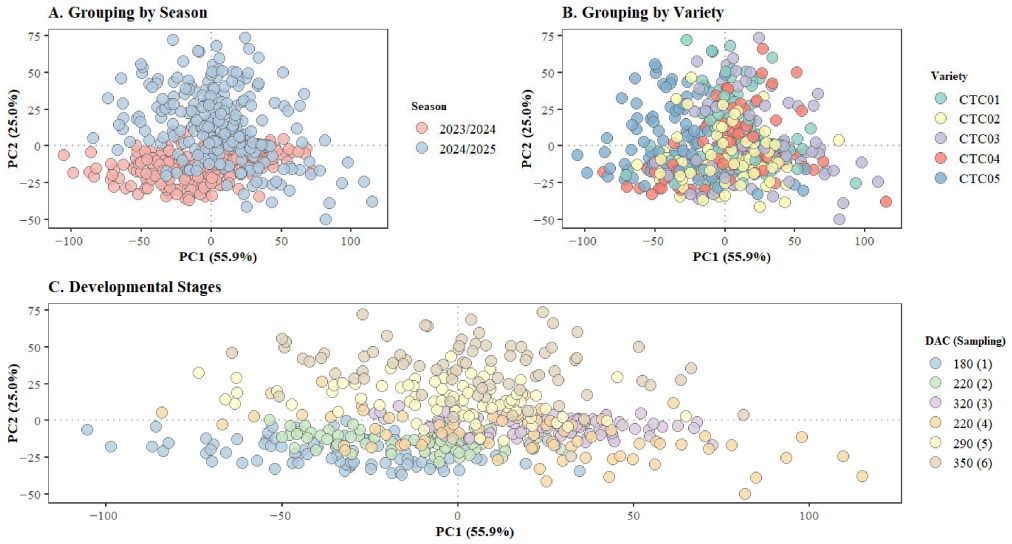

Figure 6. Principal Component Analysis (PCA) of sugarcane leaf spectral signatures, discriminated against by growing season, variety, and days after cutting (DAC).

In contrast, in the plot corresponding to varieties (Figure 6B), no defined groupings were formed, demonstrating that the genetic differences among varieties did not translate into marked changes in spectral responses. In addition to the broad overlap among varieties, CTC05 showed a slight displacement in the PCA space, suggesting a subtle spectral difference in relation to the others. However, this difference was insufficient to characterize consistent separation among varietal groups.

Finally, the plot referring to developmental stages (Figure 6C) revealed progressive grouping of the spectra according to days after cutting (DAC). In the initial stages (180–220 DAC), the points were more concentrated, reflecting greater structural and physiological homogeneity of the crop. In contrast, in the more advanced stages (290–350 DAC), greater dispersion was observed, which may be associated with changes in mesophyll structure, pigment dynamics, and other phenological effects characteristic of ripening. Overall, the PCA results indicate that sugarcane spectral variability was mainly modulated

by seasonal and phenological factors, whereas genetic differences among varieties had a limited effect on leaf reflectance.

Based on the organization observed in the PCA space, spectral variability was explored directly through the mean spectral curves, standard deviation, and coefficient of variation across the VIS–NIR–SWIR spectrum for each growing season (Figures 7 and 8). In both growing seasons, a typical vegetation spectral pattern was observed (blue line), characterized by reflectance in the visible region associated with absorption by photosynthetic pigments, a sharp increase in reflectance in the near infrared (NIR), and well-defined absorption features in the shortwave infrared (SWIR), commonly associated with water-related absorption.

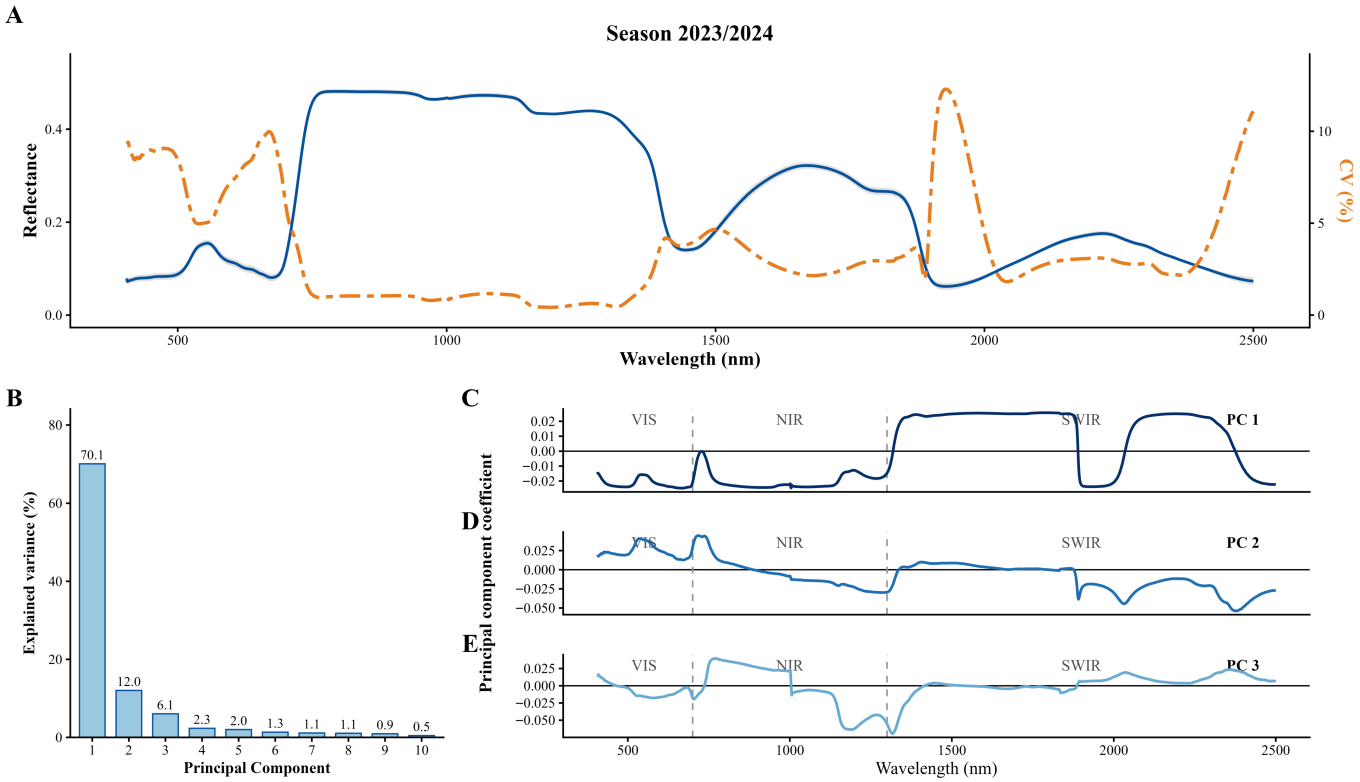

Figure 7. Mean reflectance curves across the spectrum (**A**) (blue line), accompanied by the variation range (±standard deviation, gray shaded area) and the global coefficient of variation (CV, orange dashed line). The lower panels show: (i) the variance explained by the first principal components (**B**) (PCs) and (ii) the spectral coefficients associated with the three main PCs (**C**–**E**). The background labels delineate the visible (VIS), near-infrared (NIR), and shortwave infrared (SWIR) spectral regions.

However, marked differences were observed in the amplitude of spectral variability between the growing seasons, a phenomenon strongly associated with seasonal environmental conditions and SWIR-related spectral variability. The 2023/2024 growing season showed greater overall spectral homogeneity. The season was characterized by conditions that may have favored greater spectral uniformity throughout the cycle, which may have contributed to greater spectral uniformity throughout the cycle. This context may have restricted the amplitude of spectral variation, making it more difficult to differentiate responses in the visible region, as reflected by the low coefficient of variation (CV) values in this range.

The decomposition of this variability through principal component analysis performed separately for each growing season reinforces these patterns. In the 2023/2024 growing season, the first principal component explained approximately 70% of the total spectral variance, indicating the dominance of a gradient associated with the overall reflectance

behavior across the spectrum (Figure 7B). The PC1 loadings showed a consistent contribution in the SWIR region (Figure 7C). The subsequent components captured more localized variations, with greater relative contribution from the visible and NIR regions (Figure 7D,E).

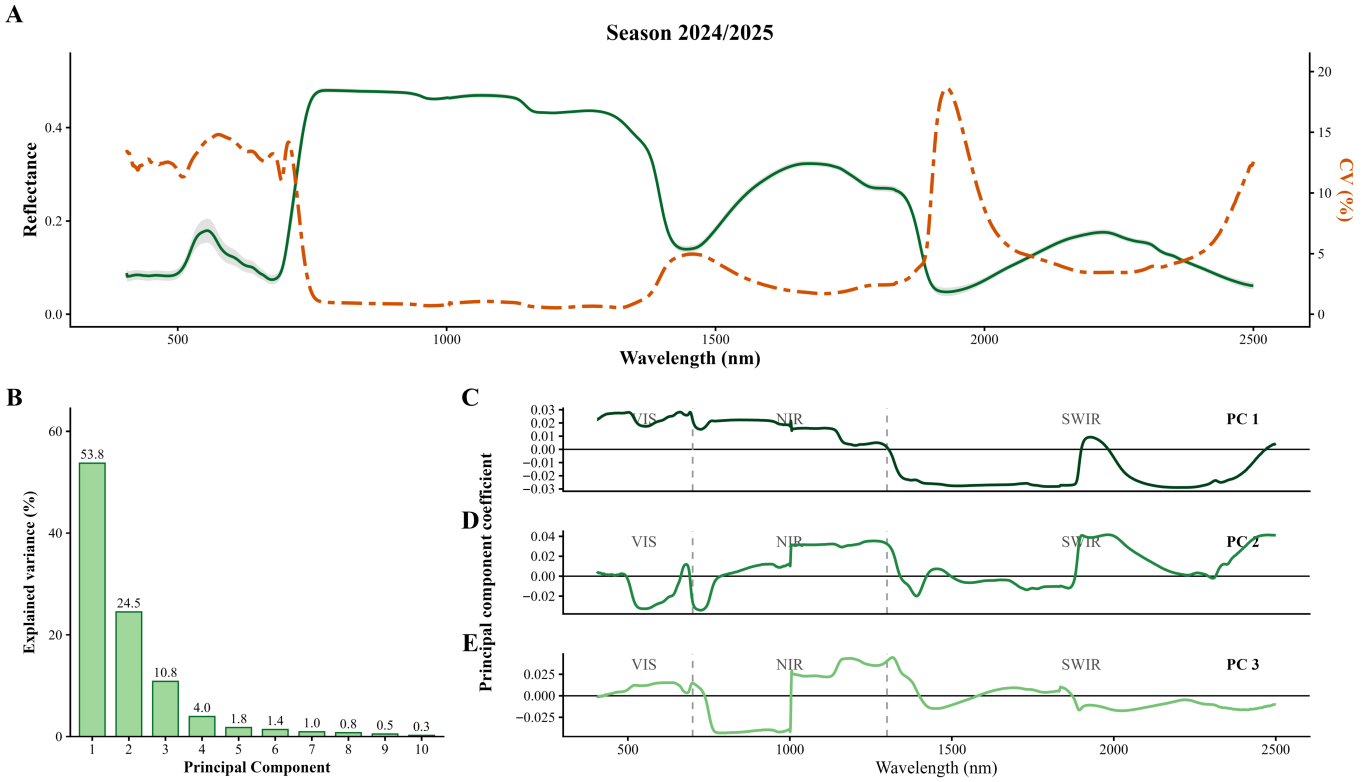

Figure 8. Mean reflectance curves across the spectrum (**A**) (green line), accompanied by the variation range (±standard deviation, gray shaded area) and the global coefficient of variation (CV, orange dashed line). The lower panels show: (i) the variance explained by the first principal components (**B**) (PCs) and (ii) the spectral coefficients associated with the three main PCs (**C**–**E**).The background labels delineate the visible (VIS), near-infrared (NIR), and shortwave infrared (SWIR) spectral regions.

In contrast, the 2024/2025 growing season exhibited greater spectral heterogeneity. Since samplings in this growing season were carried out during periods of lower rainfall, reflectance was less directly influenced by high foliar turgidity. With lower influence of water content on the overall spectral response, variation in spectral responses in the visible region (VIS) became more evident. This is evidenced by the markedly higher coefficient of variation (CV) values in this range (Figure 8A), indicating greater sensitivity to variations in nutrient concentrations.

In the 2024/2025 growing season, a redistribution of explained variance was observed, with PC1 accounting for about 53% of the total variance and PC2 contributing more than 20% (Figure 8B). This behavior indicates greater spectral complexity in this growing season, consistent with the increase in variability observed in the mean spectral curves and in the coefficient of variation. In addition, the PC1 loadings show contributions from the VIS and NIR regions, whereas for PC2 and PC3 the greatest contributions are in the NIR and SWIR regions (Figure 8C–E).

3.3. Spectral Characterization

Spectral characterization was conducted based on the visual analysis of spectra transformed by the first derivative of reflectance and by the continuum removal technique, both used to enhance spectral features associated with variation in foliar N, P, and K contents. For the first derivative, the analysis focused on the 650 to 750 nm range, corresponding in

part to the red-edge region (680–750 nm), whereas for continuum removal, the evaluation was performed predominantly between 500 and 700 nm, an interval associated with the visible region (Figures 9 and 10). To facilitate visualization of the spectral gradient and the displacement of absorption features, N, P, and K contents were grouped into distinct concentration classes based on intervals within their respective ranges. This grouping was used exclusively for the graphical representation of spectral gradients.

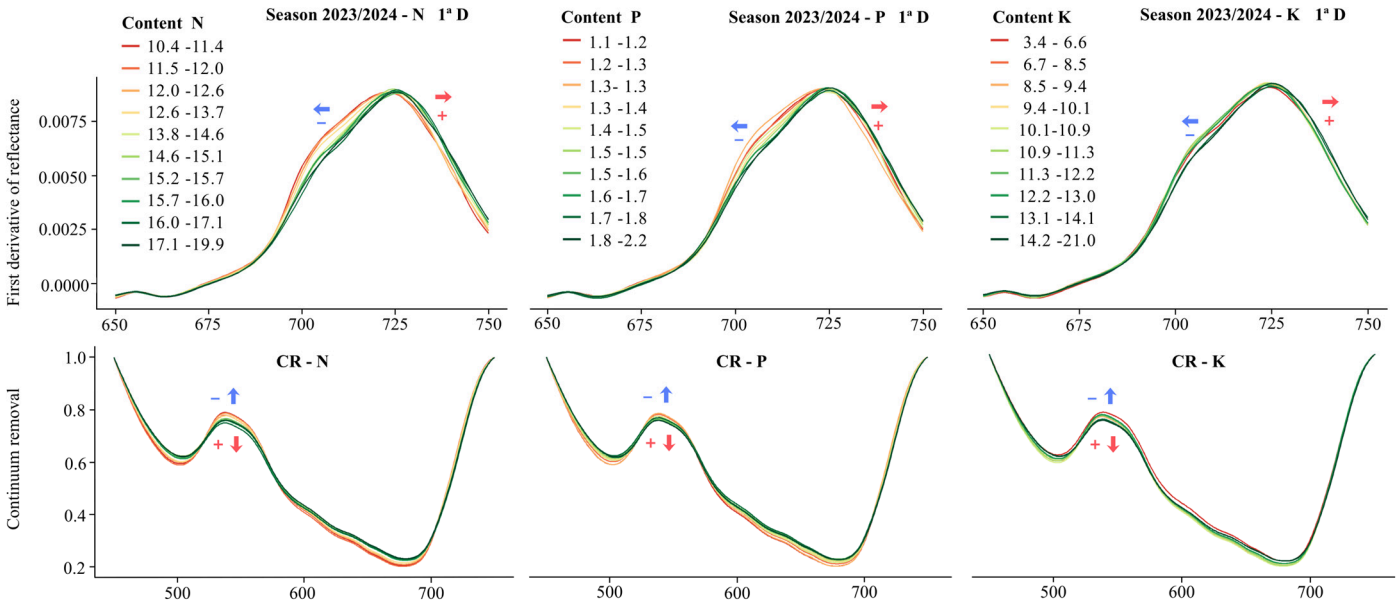

Figure 9. Spectral characterization of the 2023/2024 growing season. The panels display the first derivative (focused on the red-edge region) and continuum removal (focused on the visible region). The curves are colored according to the concentration gradients of N, P, and K, which were grouped into interval-based classes to facilitate visual interpretation. + indicates samples with higher nutrient content; − indicates samples with lower nutrient content. Arrows show the direction of spectral shift associated with increasing (+) or decreasing (−) content.

Application of the first derivative showed changes in curve slope in the red-edge region, making it possible to visually distinguish different classes of nutrient contents: a shift of the curves to the right indicated higher concentration, whereas a shift to the left indicated lower nutrient concentration. Analysis of the relative depth of absorption features in the visible region by means of continuum removal complemented these observations, demonstrating that greater absorption depth is associated with higher nutrient concentration, and vice versa.

In the 2023/2024 growing season, greater overlap among spectral curves across ranges was generally observed (Figure 9), demonstrating the effect of the spectral homogenization observed in the previous results (Figure 7). Since the plants did not experience severe restrictions in the uptake of N, P, and K during their vegetative peak, development occurred in a more balanced manner. Without the imposition of a strong limiting factor, the optical responses showed little differentiation. Although subtle trends of variation can be noted through red-edge displacement and absorption depth for nitrogen and phosphorus, where higher and lower contents follow spectral variations, the technique was not able to visually segregate K classes. Potassium, in particular, showed random behavior in this growing season, confirming the loss of spectral sensitivity under these conditions.

In contrast, the 2024/2025 growing season (Figure 10) showed separation of the curves as a function of nutrient content for both applied techniques. For nitrogen, the gradient is evident in the first derivative: samples with higher concentrations exhibited peaks of greater amplitude shifted to the right. This ordered gradient highlights the sensitivity of

the derivative in capturing the biochemical variation associated with nitrogen and, indirectly, with phosphorus and potassium. Complementarily, the continuum removal analysis reinforces this distinction. The 2024/2025 growing season exhibits more consistent visual ordering of the curves, especially for nitrogen and, to a lesser extent, for phosphorus. For potassium, although a trend toward visual organization can be observed in the transformed curves, this response was not sufficiently consistent to characterize a robust spectral relationship, as later evidenced by the correlation analysis and by the predictive performance of the models.

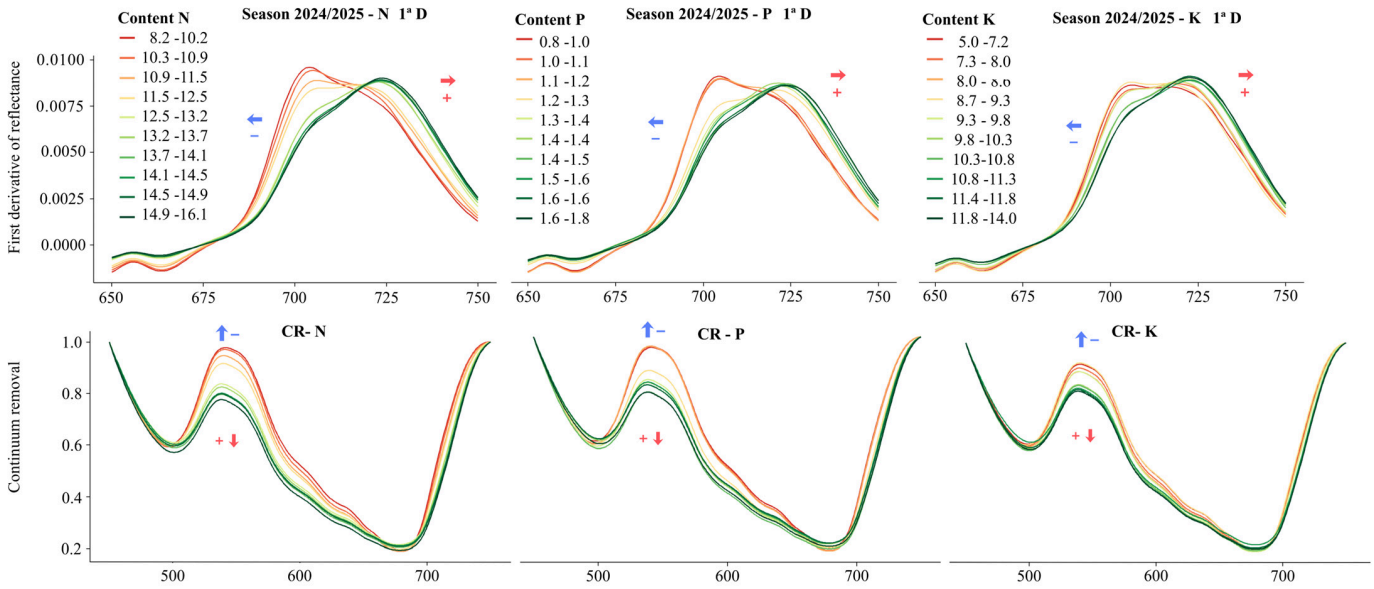

Figure 10. Spectral characterization of the 2024/2025 growing season. The panels display the first derivative (focused on the red-edge) and continuum removal (focused on the visible region), colored according to the concentration gradient of N, P, and K. The curves are colored according to the concentration gradients of N, P, and K, which were grouped into interval-based classes to facilitate visual interpretation. + indicates samples with higher nutrient content; − indicates samples with lower nutrient content. Arrows show the direction of spectral shift associated with increasing (+) or decreasing (−) content.

3.4. First Derivative and Nutritional Correlation

The application of the first Savitzky–Golay derivative was decisive for identifying consistent spectral patterns. By correcting baseline shift and eliminating background noise, the first derivative enhanced subtle absorption features, making it possible to map which regions of the spectrum are associated with nutrient contents (Figure 11).

Spearman correlation analysis revealed that, after application of the first Savitzky–Golay derivative, both growing seasons retained similar spectral patterns regarding the location of diagnostic bands, but with distinct magnitudes. The most pronounced correlations ($|r| > 0.7$) were concentrated in the visible and red-edge regions (500–750 nm), especially for nitrogen and phosphorus. Potassium, in turn, showed lower coefficients and oscillatory behavior, not reaching the adopted correlation threshold. When comparing the agricultural years, the superiority of the 2024/2025 growing season (green line) became evident. In this growing season, the correlation peaks were significantly more intense and better defined than those in the 2023/2024 growing season (orange line), especially in the visible region.

Spearman correlation analysis applied to the spectral data transformed by the first derivative made it possible to map the ranges of greatest nutritional sensitivity presented in Table 3. By establishing a strong correlation threshold ($|r| \geq 0.70$), it was verified that

the quality of the spectral response was associated with the contrasting seasonal conditions observed in each growing season, which conditioned variations in nutrient contents in the leaves. In general, the 2024/2025 growing season showed a significantly greater number of diagnostic bands and higher correlation coefficients compared with the 2023/2024 growing season, reflecting differences in spectral variability between growing seasons.

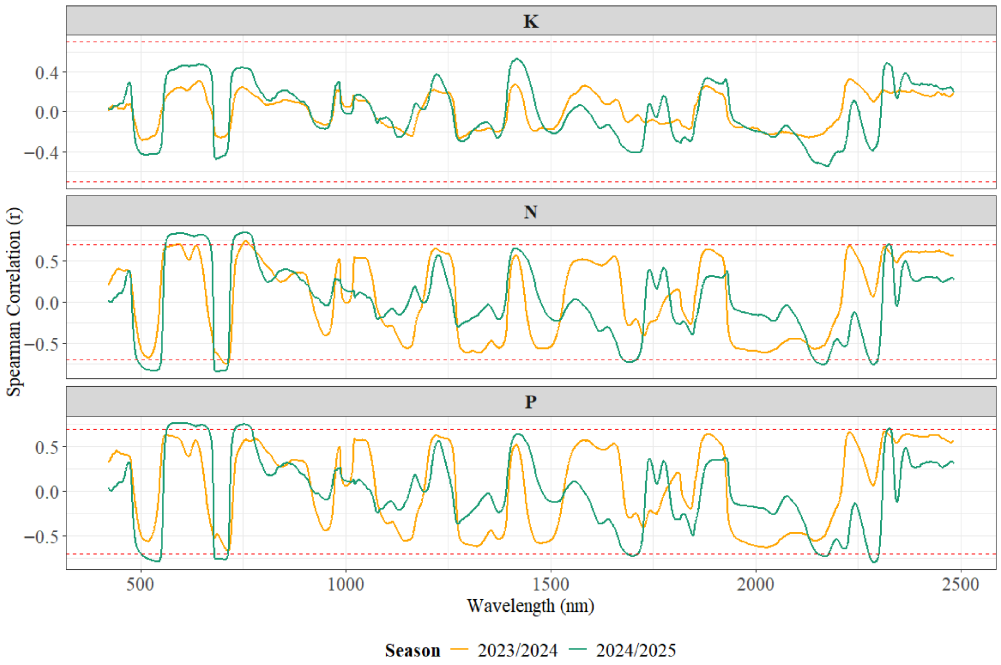

Figure 11. Spearman correlation (r) between the first derivative of reflectance and foliar potassium (K), nitrogen (N), and phosphorus (P) contents across the electromagnetic spectrum (400–2500 nm) for the 2023/2024 and 2024/2025 growing seasons. The dashed lines indicate the correlation threshold (r = 0.7).

Table 3. Spectral ranges with the highest Spearman correlation between the first derivative of reflectance and foliar N and P contents in the 2023/2024 and 2024/2025 growing seasons. * Season refers only to the 2024/2025 cycle for phosphorus (P).

Nutrient	Season	Spectral Range (nm)	Mean Correlation
N	2023/2024	619–716	−0.734
		749–765	0.728
		589–597	0.703
	2024/2025	680–714	−0.828
		725–777	0.816
		562–670	0.812
		493–550	−0.801
		2144–2176	−0.740
		2278–2297	−0.738
		1679–1709	−0.719
		2323–2327	0.703
Nutrient	*** Season**	**Spectral Range (nm)**	**Mean Correlation**
P	2024/2025	2277–2300	−0.769
		502–551	−0.759
		680–714	−0.754
		565–665	0.749
		731–770	0.737
		2152–2177	−0.721
		1686–1711	−0.716
		2323–2327	0.703

For nitrogen, a consistent response was observed in both production cycles, corroborating its strong influence on leaf reflectance due to its direct association with photosynthetic pigments. In the 2023/2024 growing season, significant correlations were concentrated in the visible and red-edge regions (589–765 nm), with mean correlation values of −0.734. However, the response in the 2024/2025 growing season was broader and more sensitive, with mean correlations greater than |r| 0.8 in the red-edge (725–777 nm) and visible (493–550 nm) regions. In addition, this nutrient showed strong correlations in the shortwave infrared (SWIR) region, specifically in the ranges 2144–2176 nm and 2278–2297 nm.

Phosphorus showed contrasting behavior. In the 2023/2024 growing season, no correlations meeting the adopted criterion were found. However, in the 2024/2025 growing season, P exhibited strong and consistent correlations, with notable overlap with nitrogen bands, mainly from 562–770 nm and 1686–1711 nm, indicating that phosphorus detection may occur indirectly.

For potassium, no continuous spectral ranges meeting the adopted correlation criterion were identified. This result indicates a less consistent spectral response for this nutrient, which may be related to its predominantly indirect physiological role in the optical properties of leaves, in contrast to nitrogen and phosphorus.

3.5. Foliar Prediction of Nitrogen, Phosphorus, and Potassium

The prediction of nitrogen, phosphorus, and potassium based on VIS–NIR–SWIR spectra using the PLSR model showed distinct performances according to the evaluated growing season. In the 2023/2024 growing season, PLSR performance was generally moderate. Coefficients of determination (R^2) of 0.67 and 0.45 were observed for nitrogen and phosphorus, respectively (Figure 12). However, for potassium, the value was negligible (R^2 = 0.04), indicating that the model was not able to explain data variability in this growing season and also showed the highest relative errors.

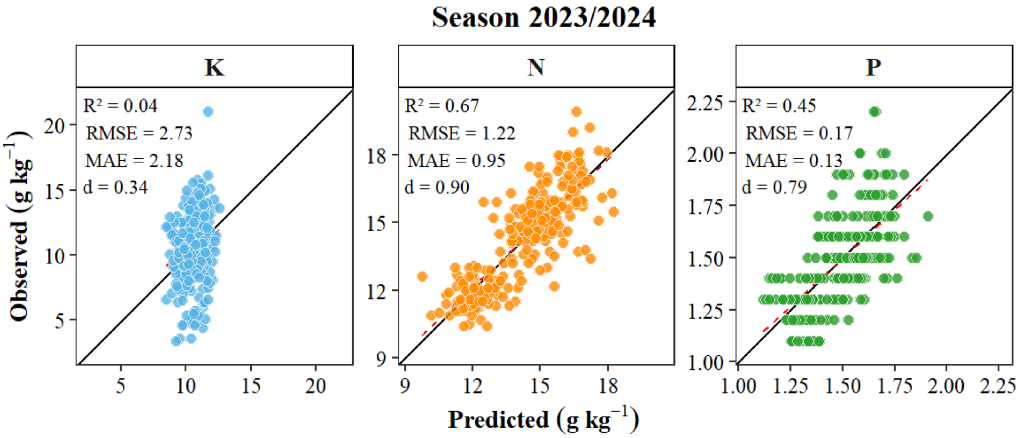

Figure 12. Performance of the prediction models for nitrogen (N), phosphorus (P), and potassium (K) in the 2023/2024 growing season. The solid black line represents the 1:1 line, and the dashed red line indicates the linear regression between predicted and observed values.

It is worth noting that RMSE and MAE for N (1.22 g kg^{-1} and 0.95) were numerically higher than those observed for P (0.17 g kg^{-1} and 0.13) due to the narrower dynamic range of the phosphorus data. The concentrations of this element were concentrated within a narrow range (1.00 to 2.25 g kg^{-1}), in contrast to the broader variation observed for nitrogen, which justifies the smaller magnitude of the absolute error metrics. In addition, the discrete levels visually observed for P in Figures 12 and 13 are associated with the analytical sensitivity and rounding procedure of the reference laboratory method used for phosphorus determination (metavanadate colorimetry). Because phosphorus occurred

within a relatively narrow absolute concentration range in the sugarcane leaf samples, the measurement resolution of the method resulted in values that appeared grouped into discrete levels in the scatterplots. This pattern does not indicate a sampling problem or data-processing error, but rather reflects the analytical precision of the reference method within the concentration range observed in this study. However, the Willmott index (d) revealed that the predictive quality for N (d = 0.9) was superior to that for P (d = 0.79), reflecting the degree to which the measured data were accurately estimated by the PLSR model.

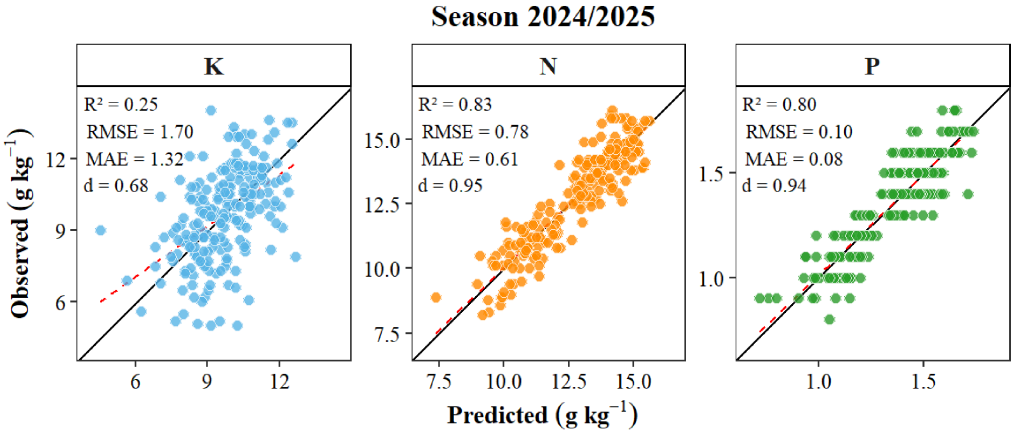

Figure 13. Performance of the prediction models for nitrogen (N), phosphorus (P), and potassium (K) in the 2024/2025 growing season. The solid black line represents the 1:1 line, and the dashed red line indicates the linear regression between predicted and observed values.

However, in the 2024/2025 growing season, the overall performance of the PLSR models was superior for all analyzed macronutrients (Figure 13). The model for N demonstrated excellent predictive ability ($R^2 > 0.8$), with reduced errors (RMSE = 0.78 g kg^{-1} and MAE = 0.61) compared with the previous growing season. Similar behavior was observed for P, which showed a marked increase in prediction performance ($R^2 = 0.80$) and lower errors (RMSE = 0.10 g kg^{-1} and MAE = 0.08). In addition, for both nutrients, d was equal to or greater than 0.94, demonstrating an excellent degree of agreement and model performance quality.

For K, although there was an improvement relative to the previous growing season, with R^2 increasing from 0.04 to 0.25 and d reaching 0.68, performance remained lower than that of the other macronutrients. This reinforces that K lacks specific absorption bands, thus presenting intrinsic challenges for prediction by reflectance spectroscopy.

4. Discussion

4.1. Factors Influencing Spectral Behavior

Among the factors affecting vegetation spectral signatures, leaf water content exerts both direct and indirect effects. The direct effects result from water absorption itself, whereas the indirect effects are related to changes in other leaf properties that vary according to hydration level and water stress. Thus, although the direct effects of water content on plant spectra are relatively straightforward to identify, interpretation becomes more complex because of the indirect effects and structural properties that vary jointly with plant water status [42].

These mechanisms alter the radiation effectively absorbed and modify the anatomical and structural properties of the leaf. The imposition of this initial stress may have contributed to the delayed vegetative development observed in the 2024/2025 growing season, which is consistent with the atypical seven-month interval between cutting and the first leaf sampling of this cycle. In addition, considering that vegetation response to

soil moisture shows a temporal lag [43], the initial conditions of the 2024/2025 season may have contributed to physiological and structural changes associated with the spectral differences observed.

The principal component analysis (Section 3.2) not only confirmed the influence of climate but also revealed the dynamics of data variability. The separation between growing seasons (Figure 6A) indicates that the set of environmental conditions associated with each cycle strongly influenced spectral variability. For varieties (Figure 6B), broad overlap was observed, suggesting that, under the conditions of this study, varietal differences were less pronounced in the PCA space. Although the CTC05 variety showed a slight displacement relative to the others, this difference was subtle and insufficient to characterize a distinct grouping. Therefore, the results indicate that the varietal effect, although detectable at low magnitude, was secondary relative to the dominant effect of environmental conditions.

Despite the overlap observed among varieties in this study, the literature indicates that genotypic distinctions may modulate the optical signature in specific spectral regions. Sordi et al. [44] demonstrated that physiological, structural, water-related, and pigment-related characteristics can promote differences in reflectance among sugarcane cultivars, especially in the visible and NIR regions. In light of this evidence, the slight displacement observed for CTC05 may reflect subtle structural or pigment-related differences; however, in the present study, these differences were not sufficiently pronounced to define consistent varietal separation in the multivariate space.

The analysis of developmental stages (DAC), in turn, revealed a pattern of progressive grouping (Figure 6C), showing that the crop spectral signature changes consistently throughout the phenological cycle. This dynamic is explained by the anatomical and biochemical changes that occur during tissue maturation: during the transition from young to mature leaves, a reduction in reflectance in the visible region is generally observed due to the accumulation of photosynthetic pigments, along with an increase in near-infrared (NIR) reflectance resulting from greater mesophyll aeration and increased air-cell interfaces, as described by Gausman et al. [45] and Bauer [46]. Subsequently, during senescence stages (end of the cycle), this pattern is reversed, with a tendency toward increased reflectance in the red region (chlorophyll degradation) and reduced reflectance in the NIR, which explains the data dispersion observed at the more advanced DACs (290–350).

In addition, the spectral signatures of sugarcane leaves reflect not only nutrient content but also structural carbohydrates, such as cellulose, hemicellulose, and lignin. Ma et al. [47] demonstrated that pretreatment with deep eutectic solvent effectively extracts lignin from wheat straw lignocellulose, highlighting the importance of understanding lignocellulosic composition for biomass valorization. In the context of spectral monitoring, variations in structural carbohydrate content during crop development, particularly the increase in lignin and the decrease in cellulose during maturation, may influence spectral signatures independently of nutrient content. This could partially explain the spectral variability observed throughout the phenological stages (Figure 6C). Future studies should consider how changes in lignocellulosic composition affect nutritional status prediction, potentially through the development of models that incorporate structural as well as compositional information.

Marked differences in the magnitude of variance between growing seasons were observed in the analysis of mean spectral curves, standard deviation, and coefficient of variation across the entire spectrum (Figures 7 and 8). In the 2023/2024 growing season, greater spectral homogeneity was observed (narrow standard deviation bands and low coefficient of variation), which may have been caused by the rainfall conditions (Figure 7A). The high percentage of variance explained by PC1 (70%) suggests a dominant reflectance gradient in the SWIR. Considering the influence of water content in the SWIR and the

rainfall context of this cycle, this gradient is consistent with variations associated with water status, suggesting that water content exerted a strong influence on spectral variation, possibly attenuating the expression of more subtle biochemical responses, such that the coefficients of variation associated with the VIS and red-edge regions were lower than those observed in the SWIR (Figure 7C).

By contrast, the 2024/2025 season exhibited greater spectral heterogeneity, with wider standard deviation bands and high coefficients of variation, especially in the visible region (Figure 8A). The lower degree of spectral homogenization associated with the water conditions of this season may have favored the optical expression of nutritional differences. The increase in coefficients of variation in the VIS region, together with the PC1 loadings showing strong weight in the VIS and NIR, indicates that the sensor captured variation in photosynthetic pigments directly related to nitrogen content (Figure 8C).

Chlorophylls a and b are the main pigments responsible for absorbing photosynthetically active radiation. They exhibit absorption peaks in the blue (430–460 nm) and red (660–675 nm) regions. These spectral ranges are directly related to photosynthetic processes and therefore reflect plant physiological activity [48].

4.2. Leaf Spectral Variability Related to Nitrogen, Phosphorus, and Potassium

Spectral characterization, performed using first-derivative and continuum-removal techniques, reflected inter-seasonal variation, especially in the visible region, which translated into differences in the strength and consistency of the spectral associations with N, P, and K. In the 2023/2024 season, a lower amplitude of spectral variation was observed in the green and red-edge regions (Figure 7A), which was reflected in curves lying closer together. As a result, only subtle changes were observed in derivative slope and in the depth of features after continuum removal for N and P, with limited visual separation between lower and higher concentration classes (Figure 9). For K, no consistent visual pattern of differentiation among nutritional levels could be identified (Figure 9).

In the 2024/2025 season, greater separation among curves was observed for the evaluated nutrients. The application of the first derivative in the red-edge region more clearly highlighted the gradient, particularly for N (Figure 10). In parallel, continuum removal reinforced the distinction among nutritional levels in the visible region (500–700 nm), where the curves showed greater ordering and contrast than those observed in the previous season, with more pronounced absorption features at higher N levels (Figure 10). For P and K, this trend should be interpreted cautiously, since the spectral response may occur more indirectly.

Previous studies have reported the visible and red-edge regions as sensitive to N variation. Silva et al. [7] and Silva et al. [25] indicated that higher N concentrations were associated with lower reflectance, that is, greater absorption. Fiorio et al. [6] and Reyes-Trujillo et al. [49] also identified these regions as sensitive to N because they are directly related to photosynthetic activity. Since N is closely linked to chlorophyll production, changes in the concentration of this nutrient directly affect the spectral signature, especially in the VIS and red-edge bands [7,49].

Furthermore, reflectance in the green and red-edge regions has been widely studied as an indicator of plant health [50–52]. For P and K, Pang et al. [53] and Silva et al. [22] also reported the visible and red-edge regions as sensitive to variation in these nutrients. For K in particular, wavelengths spanning the violet, blue, cyan, green, and yellow portions of the spectrum also showed sensitivity; however, this relationship may vary across studies.

From the Spearman correlation analysis applied to the first-derivative-transformed data, it was possible to map the spectral ranges with the greatest diagnostic sensitivity, showing that the 2024/2025 season presented a greater number of bands with strong asso-

ciation ($|r| \geq 0.70$), whereas in 2023/2024 the correlations were attenuated. This contrast between growing seasons is consistent with the environmental differences discussed earlier.

The application of the Savitzky–Golay derivative proved decisive in enhancing subtle absorption features and eliminating baseline noise. Even so, when a strong correlation threshold ($|r| \geq 0.70$) was established, a marked discrepancy between agricultural years became evident (Table 3). The 2024/2025 season exhibited a significantly greater number of diagnostic bands and higher coefficients. In 2023/2024, by comparison, the magnitude of the correlations was drastically attenuated. Unlike the subsequent cycle, the absence of strong biochemical signatures in that season was associated with tissue hydration, which homogenized the optical response.

For N, correlations exceeded $|r| > 0.80$ in the visible (493–550 nm) and red-edge (725–777 nm) regions. An important distinguishing feature of this growing season was the identification of strong correlations in the shortwave infrared (SWIR: 2144–2176 nm and 2278–2297 nm). Although nitrogen monitoring is often performed via chlorophyll in the VIS-NIR spectrum, Berger et al. [54] warned that this strategy overlooks important components, such as protein-bound N and N allocated in non-photosynthetic compartments. Therefore, the authors recommend modeling using the SWIR region in order to detect nitrogen through its protein-related indicators. Physiologically, these absorption bands are associated with proteins and nitrogen-containing compounds, responding to N-H and C-H bond vibrations [55].

The spectral regions identified as diagnostic for nitrogen and phosphorus correspond to known absorption features of chlorophyll, proteins, and phosphorus-containing compounds. However, the biochemical basis of these associations could be validated through high-resolution chemical characterization. Shi et al. [56] demonstrated the usefulness of UHPLC-Q-Exactive Orbitrap mass spectrometry for detailed chemical profiling of plant extracts, revealing the specific compounds responsible for bioactivity. Applying such chemical characterization to sugarcane leaves across different nutrient gradients could identify the specific metabolites driving spectral variations in the visible and SWIR regions, thereby providing a stronger basis for interpreting the spectrum–nutrient relationships observed here. For example, the strong correlations in the SWIR region (2144–2176 nm and 2278–2297 nm) for nitrogen likely correspond to protein-bound N and could be validated through quantitative protein analysis.

In addition, interactions between nitrogen management and other elemental cycles may have important implications for plant nutrition and stress responses. Wang et al. [57] demonstrated that nitrogen management strategies influence arsenic mobilization and nitrous oxide emissions in flooded paddy soils, highlighting the complex biogeochemical interactions that affect plant uptake. Although the present study was conducted in soils with no known contamination, similar interactions may influence spectral responses in areas where arsenic or other trace elements are present in the soil. The spectral regions identified for N prediction, particularly in the SWIR (2144–2176 nm and 2278–2297 nm), may also be sensitive to stress responses induced by elemental imbalances. Future work should explore how concurrent elemental stressors affect spectrum–nutrient relationships, potentially improving model robustness across diverse growing environments.

According to Karnieli et al. [58] and Ben-Ze'ev et al. [59], there are clear advantages to using the SWIR region for vegetation monitoring. These authors reported that SWIR has unique absorption characteristics for vegetation characterization that are absent in the VIS. In addition, from a biophysiological standpoint, healthy plants absorb more radiation in the red band because of chlorophyll and, consequently, more radiation is also absorbed in SWIR bands because of water content. This pattern was observed in the comparison between seasons, demonstrating the strong correlations found in the SWIR region for the

2024/2025 season. In 2023/2024, however, because the crop remained hydrated, this scale of variation was absent, severely attenuating the correlation coefficients.

For phosphorus, no significant correlations were found in the 2023/2024 growing season, but in 2024/2025 the nutrient exhibited strong correlations in the VNIR (562–770 nm), with broad coincidence with ranges also sensitive to N, suggesting a possible indirect component. This behavior has also been observed in other crops, such as rice, as reported by Zhang et al. [60], whose results showed that the P application rate significantly affects leaf reflectance spectra, promoting distinct changes in both the visible (350–750 nm) and near-infrared (750–1350 nm) regions. In addition, the findings of this study corroborate the results reported by Mahajan et al. [61], who found significant correlations for P in the SWIR range, specifically at 1650–1710 nm; similarly, in the present study, correlations were observed at 1686–1711 nm.

For K, no continuous spectral ranges meeting the criterion $|r| \geq 0.70$ were identified in either season, indicating a more indirect and less stable spectral response. Studies such as Pimstein et al. [62] in wheat showed that K can be retrieved under specific conditions using narrow SWIR indices and PLS, although with sensitivity to dataset variability. In rice, Yu et al. [63] identified K-sensitive bands near water absorption peaks, corresponding to 1450 and 1950 nm.

Although the spectral characterization of the 2024/2025 season showed greater visual organization of the curves also for potassium, this distinction did not translate into strong and continuous correlations across the spectrum. This result indicates that the optical response associated with K was predominantly indirect and less stable than that observed for nitrogen and phosphorus. Thus, the apparent visual separation should be interpreted cautiously, since it does not necessarily imply sufficient spectral sensitivity to support robust predictive models.

Accordingly, reflectance spectroscopy does not enable the direct estimation of foliar potassium. Its prediction occurs through indirect pathways and depends on the interactions and correlations that K establishes with other constituents [64], such as water content, chlorophyll, and other photosynthetic pigments.

4.3. Performance of Prediction Models

Model performance was consistent with the quality of the spectral response. Overall, the results followed the hierarchy of spectral sensitivity identified in the correlation analysis: Nitrogen > Phosphorus > Potassium. The comparison between agricultural years is consistent with seasonal environmental variability acting as an important factor associated with modeling robustness.

In the 2024/2025 season, the PLSR model achieved superior performance, benefiting from well-defined absorption features. In the 2023/2024 season, by comparison, the greater spectral homogenization observed in 2023/2024 limited the predictive capacity of the algorithms, resulting in lower prediction metrics (Figure 12).

For nitrogen, the model developed with data from the 2024/2025 season achieved better predictive performance (R^2 = 0.83; RMSE = 0.78 g kg^{-1}; MAE = 0.61; and d = 0.95). The superiority of this model relative to the previous 2023/2024 season (R^2 = 0.67; RMSE = 1.22 g kg^{-1}; MAE = 0.95; and d = 0.90) corroborates the importance of the spectral bands identified (Table 3). Similar studies conducted by Fiorio et al. [6] obtained comparable results (R^2 > 0.70 and RMSE < 1.41 g kg^{-1}) for nitrogen prediction in sugarcane using hyperspectral sensors. Those authors also emphasize the need to conduct studies across different periods and growing seasons to determine whether the accuracy indicators (R^2 and RMSE) remain stable. By demonstrating performance variation between the 2023/2024 and

2024/2025 seasons, the present study shows that the robustness of predictive models is strongly dependent on spectral variability.

A different pattern was observed for phosphorus, whose results varied according to the cycle. In the 2023/2024 season, the model did not show satisfactory fit (R^2 = 0.45), reflecting the lack of sensitive spectral ranges for this nutrient (Table 3). In the 2024/2025 season, however, prediction improved substantially, with the coefficient of determination reaching $R^2 > 0.80$, accompanied by low errors (RMSE = 0.10 g kg^{-1} and MAE = 0.08). The index of agreement (d > 0.94) reinforces the good performance of the model in this cycle.

However, this response should be interpreted with caution, because the literature indicates that the spectral estimation of P often occurs indirectly through physiological, pigment-related, and morphological changes triggered by phosphorus deficiency, and not necessarily through detection of a specific optical feature of the nutrient itself [65–67]. In rice, for example, P deficiency increased reflectance in the visible region and reduced reflectance in the NIR, showing that the spectral response may reflect changes in plant physiological status and foliar pigments associated with nutritional stress [60]. From this perspective, part of the high predictive capacity observed for P may be associated with its covariance with variables linked to nitrogen status and foliar chlorophyll, which reinforces the indirect nature of this spectral estimation [67]. Thus, although the model showed good predictive ability under favorable conditions, this does not necessarily imply the direct detection of a specific spectral signal of P; rather, the robustness of this prediction may depend on the stability of these indirect relationships among nutrients, growing seasons, developmental stages, and cultivation conditions.

For K, the results showed the greatest modeling difficulty among the macronutrients, regardless of the season evaluated. Although improvement occurred between the 2023/2024 and 2024/2025 cycles (R^2 from 0.04 to 0.25), performance remained low and limited. This scenario corroborates the findings of Silva et al. [22], according to whom the influence of potassium on spectral response occurs indirectly, making it difficult to establish strong correlations with leaf reflectance. These characteristics may therefore compromise the robustness of prediction models. Although the 2024/2025 season showed greater visual organization of the spectral curves, this pattern did not translate into spectral sensitivity sufficiently consistent for potassium, reinforcing that visual distinction alone is not enough to support robust predictive models for this nutrient.

This pattern may be partially explained by the chemical nature of potassium in fresh tissue: K occurs predominantly as soluble K^+ in the cell sap, especially in the vacuole and cytosol, and does not form part of the organic structures of the leaf [68,69]. Therefore, its spectral response tends to be less specific and more indirect, manifesting mainly through effects on water status, osmoregulation, and stomatal dynamics, rather than generating its own well-defined optical features [70]. In fresh leaves, this condition makes prediction even more challenging, because part of the variation associated with K may be masked by bands strongly influenced by water, especially in the SWIR [71].

The difficulty in predicting K may also be associated with the influence of water absorption bands in the spectrum. As discussed by Lu et al. [71], K plays a crucial role in regulating the osmotic pressure of guard cells. These interactions may interfere with nutrient estimation, since spectral variations in water-related bands may mask or confound the isolated detection of potassium. In addition, the authors emphasize that previous studies have not reached a unified conclusion regarding diagnostic bands for potassium monitoring. Although several spectral ranges across VIS, NIR, and SWIR have been suggested in the literature, the spectral sensitivity of K may still be masked.

The first-derivative transformation applied in this study effectively enhanced subtle absorption features, but more sophisticated feature-extraction approaches could further

improve predictive performance, particularly for challenging nutrients such as potassium (K). Dual-branch attention networks (DBAN) have shown promise for extracting diagnostically relevant features from Raman spectroscopy data [72], with parallel attention branches capturing both local spectral features and global contextual information. Adapting such architectures for VIS-NIR-SWIR spectra of sugarcane leaves could automatically learn to focus on the most informative spectral regions for each nutrient while suppressing noise from water absorption and scattering. This approach could potentially improve K prediction by learning to exploit indirect spectral associations that are not captured by linear correlation analysis.

Although PLSR proved effective for predicting N and P under optimal conditions, more sophisticated machine learning architectures could potentially improve predictive performance, particularly for K and under different environmental conditions. Graph convolutional networks have shown success in predicting complex associations in biological systems, such as herb–disease relationships [73]. Extending such graph-based approaches to spectral data could capture interactions among spectral bands and among multiple nutrients simultaneously, potentially revealing indirect relationships that are not captured by linear models. For example, the correlation between the prediction bands for P and N (Table 3) suggests shared spectral features that could be explored through multitask learning or graph-based architectures that model nutrient interdependencies.

Therefore, the sensor demonstrated sensitivity both to nutritional variation and to temporal dynamics between growing seasons. The PLSR model showed excellent performance in the 2024/2025 cycle, whereas only moderate results were obtained in the 2023/2024 season. It should be emphasized that this optical variability arises primarily from rainfall conditions and other abiotic factors, which modulate the vegetation spectral signature and, consequently, determine modeling accuracy.

The development of robust prediction models for complex industrial processes, such as copper matte smelting, requires careful consideration of process variability and multiparametric interactions [57]. Similar principles apply to the development of spectral prediction models for crop nutrition, in which multiple interacting factors, including water status, phenology, and variety, influence the spectrum–nutrient relationship. The approach used in this study, which compares model performance across different growing seasons with distinct water regimes, illustrates the importance of considering environmental variability in model development. Future studies could adopt the systematic approach used in industrial process modeling by incorporating multiple sources of variability (water, temperature, soil type) into model training in order to improve robustness under different conditions.

4.4. Implications of Variability Determinants and Limits in the Prediction of N, P, and K

The results of this study demonstrated that the spectral prediction of nitrogen (N), phosphorus (P), and potassium (K) in sugarcane was strongly conditioned by variability among growing seasons and developmental stages, in addition to limitations inherent to the optical response of these nutrients themselves. Although VIS–NIR–SWIR spectroscopy showed good potential, especially for nitrogen, spectral modeling still faces physical-optical, biological, and operational constraints that condition model performance and stability.

From a physical-optical perspective, model performance depends on the intensity and specificity of spectral interactions with leaf biochemical constituents. In the present study, this difference became evident in the greater robustness of nitrogen prediction compared with phosphorus and, especially, potassium. Nitrogen tends to exhibit more robust spectral relationships in the VIS-red-edge-NIR regions, mainly because of its association with chlorophyll and red-edge dynamics, which explains the higher accuracy reported in different studies [6,7,49]. In many scenarios, P is detected through indirect relationships

with physiological and pigment-related variables, whereas K tends to manifest through effects on water-related and structural processes, reducing the stability of diagnostic bands, as observed in this study [22,53,74,75].

From a biological perspective, genetic, structural, and physiological variation in sugarcane also affects spectral response and may reduce model specificity. In the present study, this complexity was expressed mainly in the separation between growing seasons, the progressive grouping by phenological stages, and the overlap among cultivars in the PCA space, indicating a limited varietal effect relative to seasonal and phenological factors. Differences among cultivars in leaf architecture, thickness, fiber content, and pigmentation alter reflectance in specific bands [44].

Leaf water content also modifies spectral behavior, especially in the SWIR regions, whereas phenological changes associated with biomass accumulation, pigment variation, and structural reorganization directly influence the relationships between spectrum and nutrient content [6,49]. In addition, biotic and abiotic stresses, such as pests, diseases, and water deficit, induce biophysical and biochemical changes that are reflected in the spectral signature, thereby affecting prediction accuracy [76].

In operational and practical terms, the limitations are also related to calibration and spectral processing. Factors such as sampling type and location, selected leaf, phenological stage, and sample preparation directly affect accuracy variation [6,8,27,49,77]. In addition, the choice of preprocessing methods and the quality of reference calibration condition final performance, since techniques such as MSC, SNV, and derivatives can reduce noise and enhance relevant features, but may also attenuate useful variation or introduce bias when applied without proper criteria [75,78–80].

In summary, the spectral prediction of N, P, and K in sugarcane remains conditioned by physical-optical, biological, and operational factors that alter the distribution of spectral variability among growing seasons, developmental stages, and, to a lesser extent, among varieties. Although the isolated impact of each variable was not quantified in this study, the results indicate a joint influence of these factors on model accuracy. The disparity in prediction metrics between agricultural years reinforces that changes in environmental and phenological context hinder the stabilization of a single prediction pattern across growing seasons.

5. Conclusions and Future Perspectives

VIS–NIR–SWIR reflectance spectroscopy demonstrated potential for predicting foliar macronutrient contents in sugarcane. The model performance followed a hierarchy of accuracy from nitrogen to potassium, substantiated by the quantitative metrics of the optimized model (2024/2025 season): nitrogen (R^2 = 0.83; RMSE = 0.78 g kg^{-1}), phosphorus (R^2 = 0.80; RMSE = 0.10 g kg^{-1}), and potassium (R^2 = 0.25; RMSE = 1.70 g kg^{-1}). However, model effectiveness was shown to depend on seasonal context, particularly rainfall regime. Spectral variability was modulated mainly by seasonal and phenological factors, whereas the varietal effect was limited under the conditions of this study.

The SWIR and red-edge regions stood out as informative ranges for N and, to a lesser extent, for P, suggesting associations with photosynthetic pigments, structure, and indirect covariance mechanisms. K presented the greatest challenge for modeling in both scenarios, resulting in models with low explanatory power. Consequently, its optical detection by the sensor occurs predominantly in an indirect manner, making its signal highly dependent on and easily confounded with water absorption bands in the SWIR regions.

The limited spectral sensitivity to potassium (K) observed in this study, with R^2 = 0.25 even under favorable conditions, reflects the inherent challenge of detecting K through reflectance spectroscopy due to its ionic nature and the absence of distinct

absorption features in the VIS-NIR-SWIR range. Alternative approaches using nanosensor technology offer promising solutions for K monitoring. Deng et al. [81] developed a fluorescence label-free near-infrared DNA nanosensor for monitoring extracellular potassium levels, achieving high sensitivity and selectivity through specific DNA-based recognition. The integration of such nanosensor technologies with spectroscopic platforms could provide complementary information for K monitoring in agricultural systems, potentially enabling real-time detection of K status, which is not feasible through reflectance spectroscopy alone.

Although PCA demonstrated clear spectral grouping associated with phenological stages (DAC), this study evaluated overall predictive performance using a generalized full-spectrum approach. However, it is essential to recognize that, as the sugarcane canopy matures, processes such as leaf lignification, structural thickening, and nutrient remobilization alter the internal optical pathway of leaves. Consequently, the optimal spectral bands for predicting N, P, and K are highly likely to shift dynamically throughout the vegetative cycle. We highlight this phenological spectral variation as a critical frontier for agriculture. Future research should prioritize the development of phenology-specific models by incorporating dynamic band-selection algorithms to isolate nutrient signals from structural aging effects in the crop.

Author Contributions: Conceptualization, M.L.d.S.A., I.d.L.e.L., C.A.A.C.S., M.L.S., R.R. and P.R.F.; methodology, M.L.d.S.A., I.d.L.e.L., C.A.A.C.S., M.L.S., R.R. and P.R.F.; software, M.L.d.S.A., I.d.L.e.L. and C.A.A.C.S.; validation, M.L.d.S.A., I.d.L.e.L. and C.A.A.C.S.; formal analysis, M.L.d.S.A., I.d.L.e.L., C.A.A.C.S., M.L.S., R.R. and P.R.F.; investigation, M.L.d.S.A., I.d.L.e.L., C.A.A.C.S., M.L.S., R.R. and P.R.F.; resources, P.R.F.; data curation, M.L.d.S.A., I.d.L.e.L., C.A.A.C.S. and P.R.F.; writing—original draft preparation, M.L.d.S.A., I.d.L.e.L., C.A.A.C.S., M.L.S., R.R. and P.R.F.; writing—review and editing, M.L.d.S.A., I.d.L.e.L., C.A.A.C.S., M.L.S., R.R. and P.R.F.; visualization, M.L.d.S.A., I.d.L.e.L., C.A.A.C.S., M.L.S., R.R. and P.R.F.; supervision, R.R., C.A.A.C.S. and P.R.F.; project administration, P.R.F.; funding acquisition, P.R.F. All authors have read and agreed to the published version of the manuscript.

Funding: This research was funded by Luiz de Queiroz Agricultural Studies Foundation—FEALQ, Brazil. Additional support was provided by the São Paulo Research Foundation (FAPESP, grant 2024/10366-7; Proc., 2025/18423-2 and 2025/15610-6) and by the Coordination for the Improvement of Higher Education Personnel (CAPES; Proc., 88887.027867/2024-00, 88887.993154/2024-00 and 88887.993148/2024-00).

Data Availability Statement: The data will be made available upon request.

Acknowledgments: We thank the Luiz de Queiroz Agricultural Studies Foundation (FEALQ) for funding the publication of this work. We also thank the DMLAB (Dinardo Miranda Agricultural Analysis Laboratory) for performing the chemical analyses. We also thank the São Paulo Research Foundation (FAPESP) for their support.

Conflicts of Interest: The authors declare they are not aware of any conflicts of financial interest or personal relationships that could have influenced the work reported in this article.

References

1. da Silva, L.C.; Freire, F.J.; Filho, G.M.; de Oliveira, E.C.A.; Freire, M.B.G.d.S.; Moura, A.B.; da Costa, J.V.T.; Rezende, J.S. Nutrient balance in sugarcane in Brazil: Diagnosis, use and application in modern agriculture. *J. Plant Nutr.* **2021**, *44*, 2167–2189. [CrossRef]
2. Gopalasundaram, P.; Bhaskaran, A.; Rakkiyappan, P. Integrated Nutrient Management in Sugarcane. *Sugar Tech* **2011**, *14*, 3–20. [CrossRef]
3. Som-Ard, J.; Atzberger, C.; Izquierdo-Verdiguier, E.; Vuolo, F.; Immitzer, M. Remote Sensing Applications in Sugarcane Cultivation: A Review. *Remote Sens.* **2021**, *13*, 4040. [CrossRef]
4. Jacquemoud, S.; Ustin, S.L. Leaf optical properties: A state of the art. In *8th International Symposium of Physical Measurements & Signatures in Remote Sensing*; CNES: Aussois, France, 2001; pp. 223–332.

5. Féret, J.-B.; Berger, K.; de Boissieu, F.; Malenovský, Z. PROSPECT-PRO for estimating content of nitrogen-containing leaf proteins and other carbon-based constituents. *Remote Sens. Environ.* **2021**, *252*, 112173. [CrossRef]
6. Fiorio, P.R.; Silva, C.A.A.C.; Rizzo, R.; Demattê, J.A.M.; Luciano, A.C.d.S.; da Silva, M.A. Prediction of leaf nitrogen in sugarcane (*Saccharum* spp.) by VIS-NIR-SWIR spectroradiometry. *Heliyon* **2024**, *10*, e26819. [CrossRef]
7. Silva, C.A.A.C.; Rizzo, R.; da Silva, M.A.; Caron, M.L.; Fiorio, P.R. Spatio-Temporal Generalization of VIS-NIR-SWIR Spectral Models for Nitrogen Prediction in Sugarcane Leaves. *Remote Sens.* **2024**, *16*, 4250. [CrossRef]
8. Tavares, T.R.; Fiorio, P.R.; Seixas, H.T.; Garcia, A.C.; Barros, P.P.d.S. Effects of storage on vis-NIR-SWIR reflectance spectra of Mombasa grass leaf samples. *Cienc. Rural* **2020**, *50*, e20190587. [CrossRef]
9. Durak, T.; Depciuch, J. Effect of plant sample preparation and measuring methods on ATR-FTIR spectra results. *Environ. Exp. Bot.* **2020**, *169*, 103915. [CrossRef]
10. Malavolta, E.; Vitti, G.C.; Oliveira, S.A. *Avaliação do Estado Nutricional das Plantas: Princípios e Aplicações*; Potafos: Piracicaba, Brazil, 1997.
11. Desalegn, B.; Kebede, E.; Legesse, H.; Fite, T. Sugarcane productivity and sugar yield improvement: Selecting variety, nitrogen fertilizer rate, and bioregulator as a first-line treatment. *Heliyon* **2023**, *9*, e15520. [CrossRef]
12. Roy, R.N.; Finck, A.; Blair, G.J.; Tandon, H.L.S. *Plant Nutrition for Food Security. A Guide for Integrated Nutrient Management*; FAO Fertilizer and Plant Nutrition Bulletin; Food and Agriculture Organization of the United Nations: Rome, Italy, 2006; Volume 16, pp. 201–214.
13. Clevers, J.G.P.W.; Gitelson, A.A. Remote estimation of crop and grass chlorophyll and nitrogen content using red-edge bands on Sentinel-2 and -3. *Int. J. Appl. Earth Obs. Geoinf.* **2013**, *23*, 344–351. [CrossRef]
14. Fernandes, G.C.; Rosa, P.A.L.; Jalal, A.; Oliveira, C.E.d.S.; Galindo, F.S.; Viana, R.d.S.; De Carvalho, P.H.G.; da Silva, E.C.; Nogueira, T.A.R.; Al-Askar, A.A.; et al. Technological Quality of Sugarcane Inoculated with Plant-Growth-Promoting Bacteria and Residual Effect of Phosphorus Rates. *Plants* **2023**, *12*, 2699. [CrossRef]
15. Hunsigi, G. Potassium management strategies to realize high yield and quality of sugarcane. *Karnataka J. Agric. Sci.* **2011**, *24*, 45–47.
16. Cakmak, I. The role of potassium in alleviating detrimental effects of abiotic stresses in plants. *J. Plant Nutr. Soil Sci.* **2005**, *168*, 521–530. [CrossRef]
17. Jaiswal, V.P.; Shukla, S.K.; Sharma, L.; Singh, I.; Pathak, A.D.; Nagargade, M.; Ghosh, A.; Gupta, C.; Gaur, A.; Awasthi, S.K.; et al. Potassium Influencing Physiological Parameters, Photosynthesis and Sugarcane Yield in Subtropical India. *Sugar Tech* **2021**, *23*, 343–359. [CrossRef]
18. Wang, L.; Bai, Y.-L.; Yang, L.-p. Spectral response and diagnosis of phosphorus nutrition in corn. *J. Plant Nutr. Fertil.* **2007**, *13*, 802–808. [CrossRef]
19. Wang, Z.; Skidmore, A.K.; Darvishzadeh, R.; Wang, T. Mapping forest canopy nitrogen content by inversion of coupled leaf-canopy radiative transfer models from airborne hyperspectral imagery. *Agric. For. Meteorol.* **2018**, *253–254*, 247–260. [CrossRef]
20. Acosta, M.; Quiñones, A.; Munera, S.; de Paz, J.M.; Blasco, J. Rapid Prediction of Nutrient Concentration in Citrus Leaves Using Vis-NIR Spectroscopy. *Sensors* **2023**, *23*, 6530. [CrossRef]
21. Prananto, J.A.; Minasny, B.; Weaver, T. Rapid and cost-effective nutrient content analysis of cotton leaves using near-infrared spectroscopy (NIRS). *PeerJ* **2021**, *9*, e11042. [CrossRef]
22. Silva, C.A.A.C.; Fiorio, P.R.; Rizzo, R.; Rossetto, R.; Vitti, A.C.; Dias, F.L.F.; de Oliveira, K.A.; Neto, M.B. Detection of nutritional stress in sugarcane by VIS-NIR-SWIR reflectance spectroscopy. *Cienc. Rural* **2023**, *53*, e20220543. [CrossRef]
23. Kou, J.; Duan, L.; Yin, C.; Ma, L.; Chen, X.; Gao, P.; Lv, X. Predicting Leaf Nitrogen Content in Cotton with UAV RGB Images. *Sustainability* **2022**, *14*, 9259. [CrossRef]
24. Schlemmer, M.; Gitelson, A.; Schepers, J.; Ferguson, R.; Peng, Y.; Shanahan, J.; Rundquist, D. Remote estimation of nitrogen and chlorophyll contents in maize at leaf and canopy levels. *Int. J. Appl. Earth Obs. Geoinf.* **2013**, *25*, 47–54. [CrossRef]
25. Silva, C.A.A.C.; Rizzo, R.; Oliveira, A.K.d.S.; Castro, M.P.P.; Alexandre, M.L.d.S.; Lima, I.d.L.e.; Demattê, A.M.; Fiorio, P.R. Interspecies Prediction of Nitrogen Content in Processed Plant Samples Using Spectroscopic Modeling and Transfer Learning. *Food Energy Secur.* **2026**, *15*, e70195. [CrossRef]
26. Alvares, C.A.; Stape, J.L.; Sentelhas, P.C.; Gonçalves, J.D.M.; Sparovek, G. Köppen's climate classification map for Brazil. *Meteorol. Z.* **2013**, *22*, 711–728. [CrossRef] [PubMed]
27. Lee, M.A.; Huang, Y.; Yao, H.; Thomson, S.J.; Bruce, L.M. Determining the Effects of Storage on Cotton and Soybean Leaf Samples for Hyperspectral Analysis. *IEEE J. Sel. Top. Appl. Earth Obs. Remote Sens.* **2014**, *7*, 2562–2570. [CrossRef]
28. ASD—Analytical Spectral Devices. *FieldSpec® HandHeld 2 User Manual*; ASD: Boulder, CO, USA, 2010; 93p.
29. Patel, M.K.; Padarian, J.; Western, A.W.; Fitzgerald, G.J.; McBratney, A.B.; Perry, E.M.; Suter, H.; Ryu, D. Retrieving canopy nitrogen concentration and aboveground biomass with deep learning for ryegrass and barley: Comparing models and determining waveband contribution. *Field Crops Res.* **2023**, *294*, 108859. [CrossRef]
30. Savitzky, A.; Golay, M.J.E. Smoothing and Differentiation of Data by Simplified Least Squares Procedures. *Anal. Chem.* **1964**, *36*, 1627–1639. [CrossRef]

31. R Core Team. R: The R Project for Statistical Computing, Version 4.5.2. 2025. Available online: https://www.R-project.org/ (accessed on 16 March 2026).
32. Tsai, F.; Philpot, W. Derivative Analysis of Hyperspectral Data. *Remote Sens. Environ.* **1998**, *66*, 41–51. [CrossRef]
33. Rinnan, Å.; van den Berg, F.; Engelsen, S.B. Review of the most common pre-processing techniques for near-infrared spectra. *TrAC Trends Anal. Chem.* **2009**, *28*, 1201–1222. [CrossRef]
34. De Jong, S.M. Imaging spectrometry for monitoring tree damage caused by volcanic activity in the Long Valley caldera, California. *ITC J.* **1998**, *1*, 1–10.
35. Yi, Q.-X.; Huang, J.-F.; Wang, F.-M.; Wang, X.-Z. Quantifying biochemical variables of corn by hyperspectral reflectance at leaf scale. *J. Zhejiang Univ. B* **2008**, *9*, 378–384. [CrossRef] [PubMed] [PubMed Central]
36. Wang, X.; Wang, T.; Zheng, Y.; Yin, X. Hyperspectral-attention mechanism-based improvement of radiomics prediction method for primary liver cancer. *Photodiagn. Photodyn. Ther.* **2021**, *36*, 102486. [CrossRef]
37. Silva, F.C. *Manual-de-Analises-Quimicas-de-Solos-Plantas-e-Fertilizantes-ed02-Reimpressao 2014*; Embrapa Solos: Rio de Janeiro, Brazil, 2009; 627p.
38. Hulland, J. Use of partial least squares (PLS) in strategic management research: A review of four recent studies. *Strateg. Manag. J.* **1999**, *20*, 195–204. [CrossRef]
39. Liu, W.T.H. *Aplicações de Sensoriamento Remote*; Oficina de Textos: São Paulo, Brazil, 2015.
40. Moreira, M.A. *Fundamentos do Sensoriamento Remoto e Metodologias de Aplicação*; Instituto Nacional de Pesquisas Espaciais (INPE): São José dos Campos, Brazil, 2001.
41. Castillo; Mendoza, J.; Garcés, F. *Factores Que Afectan la Calidad de la Caña de Azúcar*; Centro de Investigación de la Caña de Azúcar del Ecuador: Guayaquil, Ecuador, 2015.
42. Ollinger, S.V. Sources of variability in canopy reflectance and the convergent properties of plants. *New Phytol.* **2011**, *189*, 375–394. [CrossRef]
43. Mulianga, B.; Bégué, A.; Simoes, M.; Todoroff, P. Forecasting Regional Sugarcane Yield Based on Time Integral and Spatial Aggregation of MODIS NDVI. *Remote Sens.* **2013**, *5*, 2184–2199. [CrossRef]
44. Sordi, R.A.; Marin, F.R.; Silva, M.A.; Fiorio, P.R. Discrimination potential of sugarcane cultivars (*Saccharum* spp) through hyperspectral sensors in different production environments. *Sugar Tech* **2025**, *27*, 94–107. [CrossRef]
45. Gausman, H.W.; Allen, W.A.; Escobar, D.E. Refractive index of plant cell walls. *Appl. Opt.* **1974**, *13*, 109–111. [CrossRef]
46. Bauer, M.E. The Role of Remote Sensing in Determining the Distribution and Yield of Crops. *Adv. Agron.* **1975**, *27*, 271–304. [CrossRef]
47. Ma, H.; Fu, P.; Zhao, J.; Lin, X.; Wu, W.; Yu, Z.; Xia, C.; Wang, Q.; Gao, M.; Zhou, J. Pretreatment of Wheat Straw Lignocelluloses by Deep Eutectic Solvent for Lignin Extraction. *Molecules* **2022**, *27*, 7955. [CrossRef] [PubMed]
48. Ustin, S.L.; Jacquemoud, S. How the optical properties of leaves modify the absorption and scattering of energy and enhance leaf functionality. In *Remote Sensing of Plant Biodiversity*; Springer International Publishing: Cham, Switzerland, 2020; pp. 349–384. [CrossRef]
49. Reyes-Trujillo, A.; Daza-Torres, M.C.; Galindez-Jamioy, C.A.; Rosero-García, E.E.; Muñoz-Arboleda, F.; Solarte-Rodriguez, E. Estimating canopy nitrogen concentration of sugarcane crop using in situ spectroscopy. *Heliyon* **2021**, *7*, e06566. [CrossRef] [PubMed]
50. Ma, B.; Pu, R.; Zhang, S.; Wu, L. Spectral Identification of Stress Types for Maize Seedlings Under Single and Combined Stresses. *IEEE Access* **2018**, *6*, 13773–13782. [CrossRef]
51. Carter, G.A.; Knapp, A.K. Leaf optical properties in higher plants: Linking spectral characteristics to stress and chlorophyll concentration. *Am. J. Bot.* **2001**, *88*, 677–684. [CrossRef] [PubMed]
52. Sims, D.A.; Gamon, J.A. Relationships between leaf pigment content and spectral reflectance across a wide range of species, leaf structures and developmental stages. *Remote Sens. Environ.* **2002**, *81*, 337–354. [CrossRef]
53. Pang, Z.; Tayyab, M.; Kong, C.; Hu, C.; Zhu, Z.; Wei, X.; Yuan, Z. Liming Positively Modulates Microbial Community Composition and Function of Sugarcane Fields. *Agronomy* **2019**, *9*, 808. [CrossRef]
54. Berger, K.; Verrelst, J.; Féret, J.-B.; Wang, Z.; Wocher, M.; Strathmann, M.; Danner, M.; Mauser, W.; Hank, T. Crop nitrogen monitoring: Recent progress and principal developments in the context of imaging spectroscopy missions. *Remote Sens. Environ.* **2020**, *242*, 111758. [CrossRef] [PubMed] [PubMed Central]
55. Curran, P.J. Remote sensing of foliar chemistry. *Remote Sens. Environ.* **1989**, *30*, 271–278. [CrossRef]
56. Shi, S.; Li, K.; Peng, J.; Li, J.; Luo, L.; Liu, M.; Chen, Y.; Xiang, Z.; Xiong, P.; Liu, L.; et al. Chemical characterization of extracts of leaves of *Kadsua coccinea* (Lem.) A.C. Sm. by UHPLC-Q-Exactive Orbitrap Mass spectrometry and assessment of their antioxidant and anti-inflammatory activities. *Biomed. Pharmacother.* **2022**, *149*, 112828. [CrossRef]
57. Wang, F.; Zhang, J.; Zeng, Y.; Wang, H.; Zhao, X.; Chen, Y.; Deng, H.; Ge, L.; Dahlgren, R.A.; Gao, H.; et al. Arsenic mobilization and nitrous oxide emission modulation by different nitrogen management strategies in a flooded ammonia-enriched paddy soil. *Pedosphere* **2024**, *34*, 1051–1065. [CrossRef]
58. Karnieli, A.; Kaufman, Y.J.; Remer, L.; Wald, A. AFRI—Aerosol free vegetation index. *Remote Sens. Environ.* **2001**, *77*, 10–21. [CrossRef]

59. Ben-Ze'ev, E.; Karnieli, A.; Agam, N.; Kaufman, Y.; Holben, B. Assessing vegetation condition in the presence of biomass burning smoke by applying the Aerosol-free Vegetation Index (AFRI) on MODIS images. *Int. J. Remote Sens.* **2006**, *27*, 3203–3221. [CrossRef]
60. Zhang, Y.; Wang, T.; Li, Z.; Wang, T.; Cao, N. Based on machine learning algorithms for estimating leaf phosphorus concentration of rice using optimized spectral indices and continuous wavelet transform. *Front. Plant Sci.* **2023**, *14*, 1185915. [CrossRef]
61. Mahajan, G.R.; Sahoo, R.N.; Pandey, R.N.; Gupta, V.K.; Kumar, D. Using hyperspectral remote sensing techniques to monitor nitrogen, phosphorus, sulphur and potassium in wheat (*Triticum aestivum* L.). *Precis. Agric.* **2014**, *15*, 499–522. [CrossRef]
62. Pimstein, A.; Karnieli, A.; Bansal, S.K.; Bonfil, D.J. Exploring remotely sensed technologies for monitoring wheat potassium and phosphorus using field spectroscopy. *Field Crops Res.* **2011**, *121*, 125–135. [CrossRef]
63. Yu, Y.; Yu, H.; Li, X.; Zhang, L.; Sui, Y. Prediction of Potassium Content in Rice Leaves Based on Spectral Features and Random Forests. *Agronomy* **2023**, *13*, 2337. [CrossRef]
64. Mishra, P.; Herrmann, I.; Angileri, M. Improved prediction of potassium and nitrogen in dried bell pepper leaves with visible and near-infrared spectroscopy utilising wavelength selection techniques. *Talanta* **2021**, *225*, 121971. [CrossRef]
65. Milton, N.M.; Eiswerth, B.A.; Ager, C.M. Effect of phosphorus deficiency on spectral reflectance and morphology of soybean plants. *Remote Sens. Environ.* **1991**, *36*, 121–127. [CrossRef]
66. Siedliska, A.; Baranowski, P.; Pastuszka-Woźniak, J.; Zubik, M.; Krzyszczak, J. Identification of plant leaf phosphorus content at different growth stages based on hyperspectral reflectance. *BMC Plant Biol.* **2021**, *21*, 28. [CrossRef] [PubMed]
67. El-Mejjaouy, Y.; Belmrhar, L.; Zeroual, Y.; Dumont, B.; Mercatoris, B.; Oukarroum, A. PCA-based detection of phosphorous deficiency in wheat plants using prompt fluorescence and 820 nm modulated reflection signals. *PLoS ONE* **2023**, *18*, e0286046. [CrossRef] [PubMed]
68. Walker, D.J.; Leigh, R.A.; Miller, A.J. Potassium homeostasis in vacuolate plant cells. *Proc. Natl. Acad. Sci. USA* **1996**, *93*, 10510–10514. [CrossRef]
69. Ragel, P.; Raddatz, N.; Leidi, E.O.; Quintero, F.J.; Pardo, J.M. Regulation of K^+ Nutrition in Plants. *Front. Plant Sci.* **2019**, *10*, 281. [CrossRef]
70. Sardans, J.; Peñuelas, J. Potassium control of plant functions: Ecological and agricultural implications. *Plants* **2021**, *10*, 419. [CrossRef]
71. Lu, J.; Yang, T.; Su, X.; Qi, H.; Yao, X.; Cheng, T.; Zhu, Y.; Cao, W.; Tian, Y. Monitoring leaf potassium content using hyperspectral vegetation indices in rice leaves. *Precis. Agric.* **2019**, *21*, 324–348. [CrossRef]
72. Chen, X.; Chen, C.; Tian, X.; He, L.; Zuo, E.; Liu, P.; Xue, Y.; Yang, J.; Chen, C.; Lv, X. DBAN: An improved dual branch attention network combined with serum Raman spectroscopy for diagnosis of diabetic kidney disease. *Talanta* **2024**, *266*, 125052. [CrossRef] [PubMed]
73. Hu, X.; Lu, Y.; Tian, G.; Bing, P.; Wang, B.; He, B. Predicting Herb-disease Associations Through Graph Convolutional Network. *Curr. Bioinform.* **2023**, *18*, 610–619. [CrossRef]
74. Chen, M.; Glaz, B.; Gilbert, R.A.; Daroub, S.H.; Barton, F.E.; Wan, Y. Near-infrared reflectance spectroscopy analysis of phosphorus in sugarcane leaves. *Agron. J.* **2002**, *94*, 1324–1331. [CrossRef]
75. Zhai, Y.; Cui, L.; Zhou, X.; Gao, Y.; Fei, T.; Gao, W. Estimation of nitrogen, phosphorus, and potassium contents in the leaves of different plants using laboratory-based visible and near-infrared reflectance spectroscopy: Comparison of partial least-square regression and support vector machine regression methods. *Int. J. Remote Sens.* **2012**, *34*, 2502–2518. [CrossRef]
76. Mahlein, A.-K. Plant disease detection by imaging sensors–parallels and specific demands for precision agriculture and plant phenotyping. *Plant Dis.* **2016**, *100*, 241–251. [CrossRef]
77. Zhao, D.; Glynn, N.C.; Glaz, B.; Comstock, J.C.; Johnson, R.M. Development of leaf spectral models for evaluating large numbers of sugarcane genotypes. *Crop Sci.* **2012**, *52*, 1837–1847. [CrossRef]
78. Zheng, Y.M.; Zhang, T.Q.; Zhang, J.; Chen, X.D.; Shen, X.G. Influence of smooth, 1st derivative and baseline correction on the near-infrared spectrum analysis with PLS. *Guang Pu Xue Yu Guang Pu Fen Xi = Guang Pu* **2004**, *24*, 1546–1548. [PubMed]
79. Viscarra Rossel, R.A. ParLeS: Software for chemometric analysis of spectroscopic data. *Chemom. Intell. Lab. Syst.* **2008**, *90*, 72–83. [CrossRef]
80. Mishra, P.; Rutledge, D.N.; Roger, J.-M.; Wali, K.; Khan, H.A. Chemometric pre-processing can negatively affect the performance of near-infrared spectroscopy models for fruit quality prediction. *Talanta* **2021**, *229*, 122303. [CrossRef] [PubMed]
81. Deng, Z.; Ding, J.; Bu, J.; Li, J.; Liu, H.; Gao, P.; Gong, Z.; Qin, X.; Yang, Y.; Zhong, S. Fluorophore Label-Free Light-up Near Infrared Deoxyribonucleic Acid Nanosensor for Monitoring Extracellular Potassium Levels. *Anal. Chem.* **2024**, *96*, 4023–4030. [CrossRef] [PubMed]

Disclaimer/Publisher's Note: The statements, opinions and data contained in all publications are solely those of the individual author(s) and contributor(s) and not of MDPI and/or the editor(s). MDPI and/or the editor(s) disclaim responsibility for any injury to people or property resulting from any ideas, methods, instructions or products referred to in the content.